

1
2
3
4
5
6
7
8
9
10
11
12
13
14
15
16
17
18
19
20
21
22

Single Cell Enhancer Activity Maps Neuronal Lineages in Embryonic Mouse Basal Ganglia

Linda Su-Feher^{1,2,12}, Anna N. Rubin^{3,12}, Shanni N. Silberberg³, Rinaldo Catta-Preta^{1,2,11},
Kenneth J. Lim^{1,2,3}, Iva Zdilar^{1,2}, Christopher S. McGinnis⁴, Gabriel L. McKinsey⁵,
Thomas E. Rubino, Jr.^{1,2}, Michael Hawrylycz⁶, Carol Thompson⁶, Zev J. Gartner^{4,7,8,9},
Luis Puelles¹⁰, Hongkui Zeng⁶, John L. R. Rubenstein^{3#}, Alex S. Nord^{1,2#}

¹Department of Psychiatry and Behavioral Sciences, University of California, Davis, Davis, California, USA. ²Department of Neurobiology, Physiology and Behavior, University of California, Davis, Davis, California, USA. ³Nina Ireland Laboratory of Developmental Neurobiology, Department of Psychiatry, University of California, San Francisco Medical School, San Francisco, California, USA. ⁴Department of Pharmaceutical Chemistry, University of California, San Francisco, San Francisco, CA, USA. ⁵Department of Pediatrics, University of California, San Francisco, San Francisco, USA. ⁶Allen Institute for Brain Science, Seattle, WA, USA. ⁷Helen Diller Family Comprehensive Cancer Center, San Francisco, CA, USA. ⁸Chan Zuckerberg BioHub, University of California San Francisco, San Francisco, CA, USA. ⁹Center for Cellular Construction, University of California San Francisco, San Francisco, CA, USA. ¹⁰Department of Human Anatomy and Psychobiology and IMIB-Arrixaca Institute, University of Murcia, Spain. ¹¹Current address: Department of Genetics, Blavatnik

23 Institute, Harvard Medical School, Boston, Massachusetts, USA. ¹²These authors
24 contributed equally.

25

26 #Correspondence to Alex S. Nord (asnord@ucdavis.edu) and John L. R. Rubenstein
27 (john.rubenstein@ucsf.edu).

28 **Abstract**

29

30 Enhancers integrate transcription factor signaling pathways that drive cell fate
31 specification in the developing brain. We used single cell RNA-sequencing (scRNA-seq)
32 to capture enhancer activity at single cell resolution and delineate specification of cells
33 labeled by enhancers in mouse medial, lateral, and caudal ganglionic eminences (MGE,
34 LGE, and CGE) at embryonic day (E)11.5. We combine enhancer-based reporter
35 labeling with single-cell transcriptional readout to characterize enhancer activity and
36 define cell populations in vivo. Seven enhancers had diverse activities in specific
37 progenitor and neuronal populations within the GEs. We then applied enhancer-based
38 labeling, scRNA-seq, and analysis of in situ hybridization (ISH) data to distinguish
39 subtypes of MGE-derived GABAergic and cholinergic projection neurons and
40 interneurons. This work demonstrates how the power of scRNA-seq can be extended by
41 enhancer-based labelling and leveraging ISH data and reveals novel lineage
42 specification paths underlying patterning of developing mouse brain.

43 **Introduction**

44

45 During brain development, transcriptional programs governed by the genomic interplay
46 of transcription factors and cis-regulatory enhancer and promoter sequences drive the
47 proliferation and specification of neuronal and glial lineages (Beccari et al., 2013; Nord,
48 2015). An understanding of this regulatory symphony in the telencephalon has been
49 derived via decades of genetic dissection of transcription factor signaling (Kessarar et
50 al., 2014; Lim et al., 2018; Long et al., 2009), more recently extended via genomic
51 approaches (Lindtner et al., 2019; Sandberg et al., 2016), and is now undergoing a
52 revolution via application of single cell RNA-sequencing (scRNA-seq). scRNA-seq has
53 produced fine-scale elucidation of cell types in the mammalian brain (Zeisel et al.,
54 2018); however, major challenges remain towards understanding the dynamics of cell
55 state and identity that occur in the context of neurodevelopment.

56

57 The embryonic basal ganglia (BG) include spatially distinct proliferative zones of the
58 ganglionic eminences (GEs), which include the medial, lateral, and caudal ganglionic
59 eminences (MGE, LGE, and CGE) (J.L.R. and Campbell, 2020). Progenitor cells in the
60 ventricular (VZ) and subventricular (SVZ) domains in the GEs give rise to many
61 neuronal classes. Neuron types that originate in embryonic BG include GABAergic
62 projection neurons and cholinergic neurons (Fragkouli et al., 2009) that form the ventral
63 pallidum, globus pallidus (Flandin et al., 2010; Nóbrega-Pereira et al., 2010), and striatal
64 structures (J.L.R. and Campbell, 2020) that make up the mature BG. In addition, the
65 GEs generate interneurons that populate the striatum, cortex, olfactory bulb, and other

66 brain regions (Anderson et al., 1997; Batista-Brito et al., 2020; Lim et al., 2018; Marín et
67 al., 2000). Building on bulk transcriptomics and in situ hybridization studies (ISH),
68 scRNA-seq has been applied to embryonic mouse BG, revealing generalized progenitor
69 populations and early born GABAergic lineages, with a focus on cortical interneuron
70 (CIN) specification (Mayer et al., 2018; Mi et al., 2018). While CINs are one major
71 output of embryonic BG, single cell characterization of GABAergic and cholinergic as
72 well as early born CIN lineages and that arise in the BG remains largely unexplored.
73 Resolving the early stages of BG neurogenesis via scRNA-seq and ISH has been
74 limited by major barriers: paucity of region- and lineage-specific single gene markers,
75 similarity of early transcriptional programs, spatial mixing of progenitors within germinal
76 zones and immature cell types in the MZ, and regional organization of BG neurogenesis
77 that has been poorly captured by unguided scRNA-seq analysis.

78

79 Fate mapping via reporter labeling has provided critical insights into the origins of
80 neuronal cell populations (Batista-Brito et al., 2020). Notably, enhancers drive highly
81 specific transcription patterns, including in the developing telencephalon (Visel et al.,
82 2013), thus offering exciting possibilities for cell-type specific labeling and genetic
83 manipulation. We previously demonstrated the utility of enhancer-driven transgenic
84 reporter mouse lines for fate mapping and genetic manipulation of neuronal populations
85 originating in embryonic BG and cortex (Pattabiraman et al., 2014; Silberberg et al.,
86 2016). We generated transgenic mice harboring evolutionarily conserved enhancer
87 sequences that drive expression of CreER^{T2} and GFP. These developmental enhancers
88 exhibited spatiotemporal activity across expression domains within the embryonic BG

89 and mark early cell populations prior to terminal cell fate commitment. Enhancers
90 differentially labeled cell populations that spatially intermingle and alternatively marked
91 regionally distinct mitotic and postmitotic populations during development. Fate mapping
92 with these enhancer-driven CreER^{T2}-GFP mice demonstrated that developmental
93 lineages marked by transient enhancer activity produce varied mature neuron
94 populations within and across these enhancers. Importantly, beyond their use in
95 understanding neuronal lineages, these enhancer-driven reporter lines offer the
96 opportunity for function-based analysis of dynamic in vivo enhancer activity, a missing
97 feature from studies modeling enhancer activity via epigenomic approaches. More
98 broadly, enhancer-based cell labeling is emerging as a powerful tool for cell-type
99 identification, enrichment, and modulation in neuroscience and other areas, yet little
100 remains known about sensitivity and specificity of enhancer-driven reporter expression
101 at single cell resolution.

102

103 In this study, we apply the novel strategy of pairing enhancer-based transgenic reporter
104 mouse lines with scRNA-seq to define specific enhancer-labeled lineages at single cell
105 resolution in early embryonic BG. These experiments reveal functionally defined distinct
106 enhancer activities across scRNA-seq-defined cell states and lineages. Next, we
107 focused on the MGE and integrated ISH mapping of transcript expression from the Allen
108 Developing Mouse Brain Atlas (ABA) (Lein et al., 2007) to provide a higher resolution
109 anatomical definition of lineages identified by enhancer-labeling and scRNA-seq. Our
110 study identified proliferative and postmitotic cells that are distinctly labeled by enhancers

111 active in MGE, LGE, and CGE and revealed novel specification paths for enhancer-
112 labeled and spatially defined populations of early BG-derived neuronal lineages.

113

114 **Results**

115

116 **Comparative activity of seven enhancers in E11.5 BG via scRNA-seq**

117

118 We profiled enhancer-labeled cell populations from day (E)11.5 MGE, LGE, or CGE
119 across seven subpallial enhancer transgenic mouse lines (Silberberg et al., 2016)
120 (Figure 1A). The selected transgenic lines express GFP and CreER^{T2} with enhancer-
121 driven divergent patterns in the ventricular (VZ), subventricular (SVZ), and mantle (MZ)
122 zones of the GEs. These enhancers are putatively associated with developmentally
123 expressed genes and have restricted regional activity within the GEs at E11.5,
124 summarized in Figure 1B. The objective of these experiments was threefold. First, to
125 establish the utility and sensitivity to detect enhancer-driven reporter expression via
126 scRNA-seq. Second, to define and compare representative enhancer activities and
127 enhancer-labeled progenitors and early neuronal populations across MGE (enhancers
128 *hs1538*, *hs1056*, *hs799*, and *hs192*), LGEs (*hs841* and *hs599*), and CGE (*hs841* and
129 *hs953*) at E11.5. Third, to resolve fine-scale differences among cells labeled by
130 regionally distinct MGE progenitor-associated enhancers (*hs1538* and *hs1056*) and
131 early neuronal enhancers that differentially label emerging lineages (*hs799* and *hs192*).

132

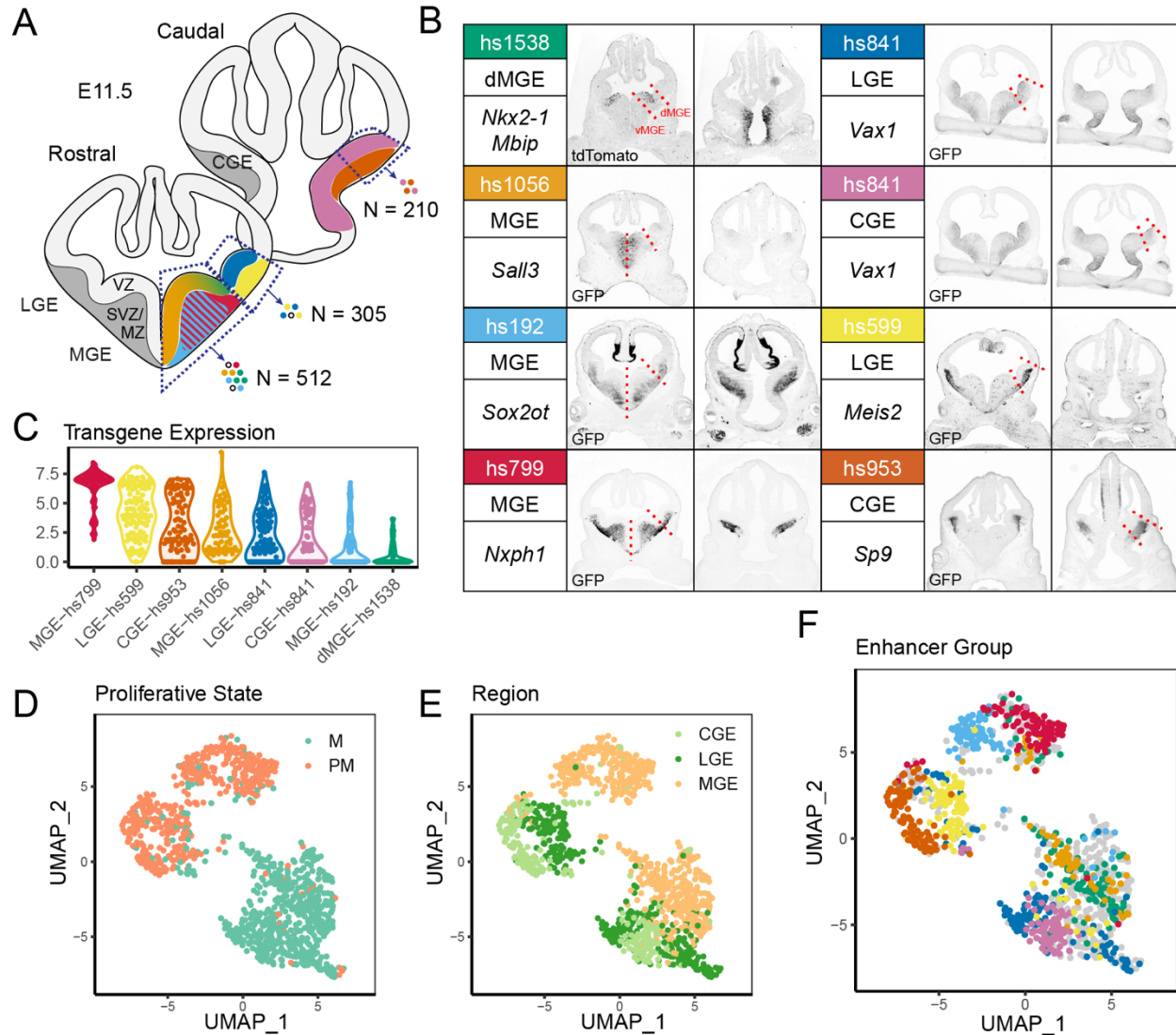


Figure 1: Profiling enhancer-labeled single cells in E11.5 basal ganglia.

(A) Schematic of dissection, with colors representing the activity of seven transgenic enhancer reporters characterized using C1 scRNA-seq. CGE: caudal ganglionic eminence; LGE: lateral ganglionic eminence; MGE: medial ganglionic eminence; VZ: ventricular zone; SVZ: subventricular zone; MZ: mantle zone. (B) Summary of the seven enhancers profiled, including dissection region, putative gene regulatory target, and representative GFP immunohistochemistry (IHC) imaging of enhancer transgenic reporters at E11.5, depicting activity within the ganglionic eminences. Red lines indicate microdissection boundaries. GFP IHC images are adapted from (Silberberg et al., 2016). (C) Violin plot of normalized transgene expression by enhancer group. (D) Visualization of single cells by UMAP, colored by mitotic state (green: M, mitotic; orange: PM, postmitotic). (E) Visualization of single cells by UMAP, colored by region of dissection (light orange: MGE; light green: CGE; dark green: LGE). (F) Visualization of single cells by UMAP, colored by transgenic enhancer grouping. Colors correspond to header colors in (B). Enhancer-negative cells are depicted in grey.

134 Using the seven transgenic lines, we performed targeted BG microdissection and
135 preparation of reporter-positive and ungated single cells. Single cell suspensions were
136 either first segregated for transgene expression through fluorescence activated cell
137 sorting (FACS, Figure S1) or passed directly to the Fluidigm C1 system for capture and
138 amplification of the transcriptomes of individual cells. The regional dissections included:
139 for *hs599* the LGE; for *hs953* the CGE; for *hs1538* the dorsal (d)MGE; and for *hs1056*,
140 *hs192*, and *hs799*, the MGE. For one enhancer, *hs841*, we independently dissected the
141 LGE and CGE. For *hs1538*, we used CreER^{T2}-driven tdTomato signal via cross to Ai14
142 reporter mice (Madisen et al., 2010) for gating due to low GFP signal. For details
143 regarding sample preparation, see Table S1. After sequencing and quality control
144 (Figure S2A-L), 1027 cells were included for analysis, with ~594,000 reads and ~5,140
145 genes per cell on average.

146

147 Our first objective was to demonstrate the feasibility of single cell enhancer activity
148 mapping by establishing whether enhancer-driven transgene expression could be
149 mapped to single cells via scRNA-seq. We used a combination of FACS⁺ gating and
150 transgene (CreER^{T2}-IRES-GFP or tdTomato) RNA expression to assign cells as
151 enhancer-positive or negative (“None”). 315 cells were unsorted or FACS⁻ and
152 transgene negative; 712 cells were FACS⁺ and/or expressed non-zero transgene.
153 Based on tissue dissection and enhancer line, enhancer-positive cells were assigned to
154 one of eight categories: MGE-*hs1056*, MGE-*hs1538*, MGE-*hs192*, MGE-*hs799*, LGE-
155 *hs599*, CGE-*hs953*, LGE-*hs841*, and CGE-*hs841*. Enhancer-labeled cells generally
156 exhibited expression of presumed target genes with some exceptions. Enhancer-driven

157 reporter transcripts were detectable at single cell resolution across all enhancers, with
158 variation in presence and transcript level captured via scRNA-seq (Figure 1C). Five of
159 the seven enhancers exhibited strong concordance between reporter protein GFP⁺
160 gating and transgene transcript detected via scRNA-seq (Figure S2M). The other two
161 lines, dMGE-*hs1538* and MGE-*hs192*, had weaker sensitivity, with 30-40% of FACS
162 reporter-positive cells having detectable transgene transcript. Nonetheless, even for
163 enhancers with weaker transcriptional activity, reporter transgene was reliably detected
164 via scRNA-seq in a substantial fraction of FACS-determined reporter-positive cells,
165 demonstrating the overall utility of this approach for function-based scRNA-seq
166 enhancer activity profiling.

167

168 **TF expression organizes scRNA-seq data by proliferative state and BG region**

169

170 Using highly variable genes in scRNA-seq analysis is a common approach for feature
171 selection (Butler et al., 2018); however, this method did not adequately separate
172 regional and cell state identity in our data (Figure S3). As an alternative, we used a
173 transcription factor (TF)-curated approach, with the rationale that TFs drive lineage
174 specification and cell identity. We rooted this analysis using 689 TFs profiled for RNA
175 ISH patterns at E11.5 and E13.5 in the Allen Developing Mouse Brain Atlas (ABA) (Lein
176 et al., 2007) (Table S2, Figure S4A-B). 455 of these TFs were expressed in our E11.5
177 scRNA-seq data, of which 292 (64.2%) had detectable ISH expression in the BG
178 (Figure S4C-E). We used these 455 TFs to define scRNA-seq cell identity and for visual
179 representation via UMAP plots (Figure 1D-F). Using this TF-curated approach,

180 proliferative state and regional origin were the primary aspects of scRNA-seq variation
181 (Figures 1D-E). We compared TF-curated analysis to results using highly variable
182 genes (Figures S3A-C), before and after performing regression analysis to reduce the
183 influence of cell cycle phase (Figures S3D-F). Excluding non-TFs reduced the
184 contribution of cell cycle phase and confounding sources of variation (e.g. sequencing
185 batch) to cell clustering and improved separation by GE origin (Figure S3G-I).

186

187 **Enhancers label cells with specific regional identities and developmental** 188 **trajectories**

189

190 Having shown that scRNA-seq can reliably identify enhancer-positive cells and that our
191 TF-curated approach enables separation across regional origin and proliferative states,
192 we next modeled transcriptional differences across enhancer-positive cells. First, we
193 modeled transitional cell states via diffusion mapping. Second, we examined differences
194 across cluster-based transcriptional identities. We identified two major diffusion
195 components (DC) corresponding to proliferative state (DC1) and MGE from LGE/CGE
196 origin (DC2) (Figure 2A-F). DC1 captured the stem cell, proneural, and neurogenic
197 transition, with genes such as *Hes1*, *Ccnd2*, *Gadd45g*, and *Slc34a2* marking cells at
198 various stages of this transition (Figure 2G). Lower values of DC2 were associated with
199 MGE identity, marked by expression such MGE-specific genes such as *Nkx2-1*, *Lhx6*,
200 and *Lhx8* (Flames et al., 2007) (Figure 2G). Higher values of DC2 were associated with
201 LGE or CGE identity (Figure 2D,F). DC2 diversity was driven by expression of region-
202 defining TFs such as *Nkx2-1* in the MGE and *Pax6* in the CGE and LGE (Figure 2G,I).

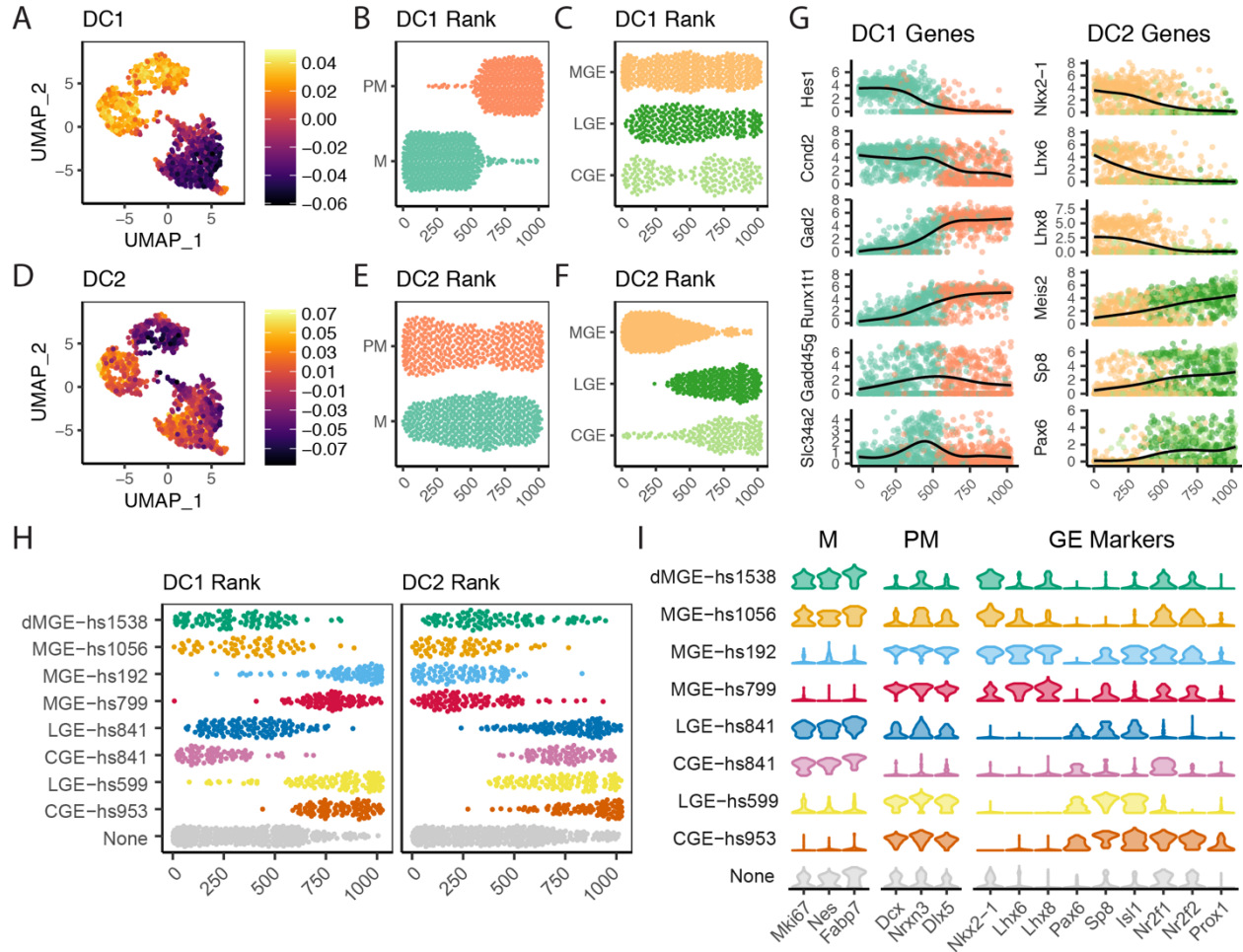


Figure 2: Diffusion mapping reveals progenitor state and regional identity gradients.

(A,D) UMAP colored by diffusion component value (DC)1 (A) or DC2 (D). (B,E) Cells ranked by DC1 (B) or DC2 (E) value, separated and colored by mitotic state. (C,F) Cells ranked by DC1 (B) or DC2 (E) value, separated and colored by ganglionic eminence. (G) Relative expression of differentially expressed genes across DC1 (left) or DC2 (right). Cells on x-axis are ordered by DC1 or DC2 rank. Line represents generalized additive model (gam) line. (H) Cells ranked by DC1 (left) or DC2 (right) rank, separated and colored by enhancer group. (I) Violin plots of relative expression by enhancer group for marker genes associated with mitotic identity (M), postmitotic identity (PM), and various markers with ganglionic eminence-associated expression.

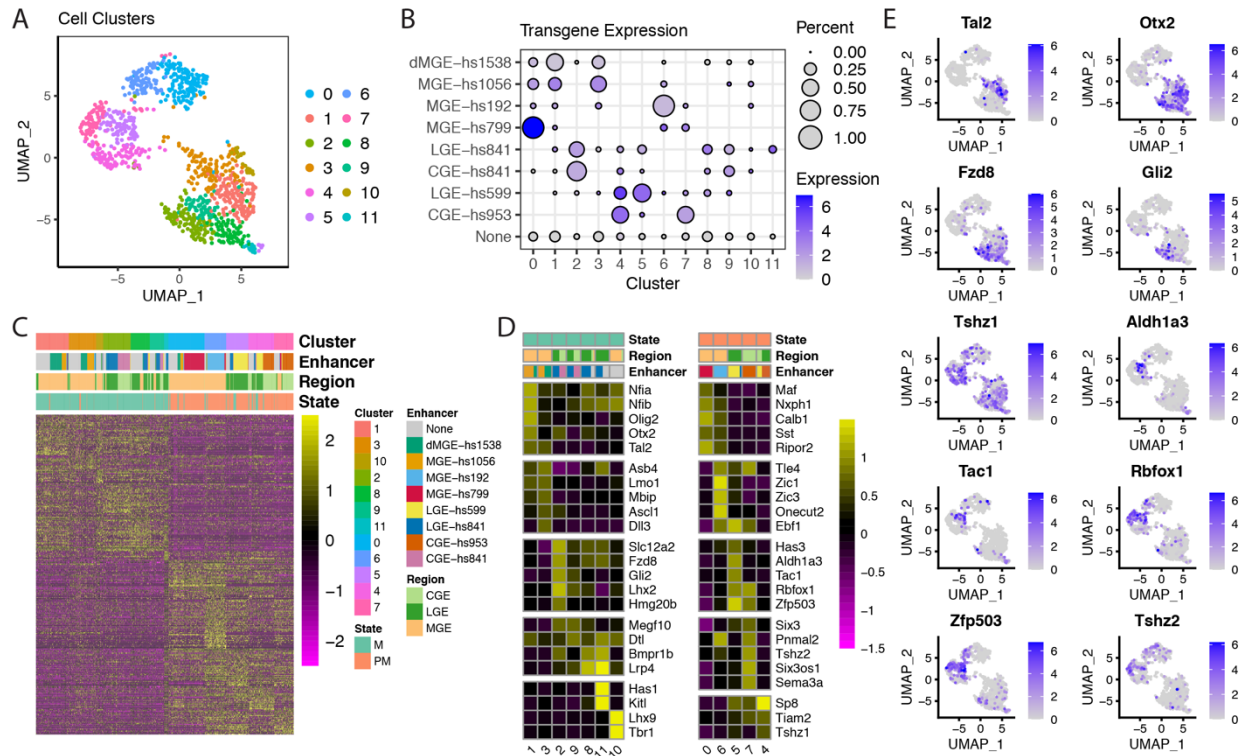
203 The strongest separation of LGE and CGE identity are the caudal-biased TFs *Nr2f1* and
 204 *Nr2f2* (Hu et al., 2017) (Figure 2I). DC1 and DC2 values distinguished cells labeled by
 205 different enhancers and indicate that these developmental enhancers are active across
 206 maturation states within the GEs (Figure 2H). VZ-associated enhancers *dMGE-hs1538*,
 207 *MGE-hs1056*, and CGE- and LGE-*hs841* labeled cells across the proliferative zone of

208 DC1, indicating enhancer activity across multiple maturation states (Figure 2H). In
209 contrast, SVZ/MZ-associated enhancers MGE-*hs192*, MGE-*hs799*, LGE-*hs599*, and
210 CGE-*hs953* labeled cells across the postmitotic zone of DC1, indicating these
211 enhancers are active across neuronal maturation (Figure 2H).

212

213 We next performed clustering using TF-curated scRNA-seq expression, identifying 12
214 cell clusters that separated by proliferative state and regional or cell-type identity (Figure
215 3A, Table S3). We further used random forest classification to define informative
216 transcripts that discriminate cells labelled by specific enhancers (Table S4). Cells
217 labeled by enhancers dMGE-*hs1538*, MGE-*hs1056*, CGE-*hs841* and LGE-*hs841*
218 primarily grouped into mitotic clusters (cl)-1, cl-2, cl-3, cl-8, and cl-9, further separated
219 by regional identity (MGE versus non-MGE). Within these regional boundaries, VZ/SVZ-
220 associated enhancers split across multiple clusters (Figure 3B), paralleling diffusion
221 mapping results suggesting mitotic enhancers label multiple proliferative states.
222 Compared to enhancers with progenitor activity, enhancers active in postmitotic cells
223 (MGE-*hs192*, MGE-*hs799*, LGE-*hs599*, and CGE-*hs953*) were biased toward specific
224 cell type clusters within broader regional identities (Figure 3B). To characterize cell
225 types that were differentially labeled by these enhancers, we performed differential gene
226 expression analysis using the full transcriptome of 17,015 expressed genes to identify
227 differentially expressed (DE) genes for each TF-defined cluster (Figure 3C-E).

228



229 Proliferative clusters cl-1, 3, 2, and 9 encompassed proliferating cells including those
 230 labeled by VZ/SVZ-associated enhancers *MGE-hs1538*, *MGE-hs1056*, and CGE- and
 231 *LGE-hs841*. The mitotic-associated enhancers captured both early VZ and SVZ cells.
 232 Cells in cl-1 expressed neural stem cell markers including higher expression of *Nfia*,
 233 *Nfib*, and *Olig2* (Figure 3D). Cl-3 was associated with higher levels of intermediate
 234 progenitor markers such as *Asb4* and *Ascl1*. Proliferative LGE and CGE cells from
 235 *hs841* comprised the majority of cl-2 and cl-9 and expressed VZ markers including *Lhx2*

236 and *Fzd8*. Enhancer-negative LGE and LGE-*hs841* mitotic cells additionally form
237 clusters cl-8 and cl-11, which expressed genes such as *Lrp4*, *Has1*, and *Kitl*. Cl-10 was
238 composed primarily of enhancer-negative MGE cells and expressed *Lhx9* and *Tbr1*,
239 indicative of cortical or diencephalic rather than basal ganglia identity. From random
240 forest classification, markers that distinguished LGE, CGE, and MGE progenitor-
241 associated enhancers recapitulated region-associated TFs from DC2 (Table S4). MGE
242 rostradorsal (*hs1538*) and caudoventral (*hs1056*) biased enhancers were distinguished
243 by quantitative differences across TFs including *Otx2* and *Id4*, identifying TF expression
244 gradients that distinguished progenitor cells across MGE regional axes.

245

246 Compared to proliferative enhancers, postmitotic enhancers active in SVZ/MZ mapped
247 to distinct transcriptional clusters corresponding to emerging neuron types. LGE-*hs599*
248 and CGE-*hs953* are both represented in cl-4, which expressed higher levels of genes
249 including *Sp8*, *Tiam2*, and *Tshz1* (Figure 3D-E), suggesting cl-4 is more immature than
250 cl-5 and cl-7 and has not yet acquired strong LGE or CGE regional specificity. Cl-5,
251 composed predominantly of LGE-*hs599* cells, expressed genes including *Rbfox1*, *Tac1*,
252 and *Zfp503*. Cl-7, composed predominantly of CGE-*hs953* and enhancer-negative cells,
253 expressed genes such as *Six3*, *Tshz2*, and *Sema3a*. Genes defining these clusters
254 shared general markers of early GABAergic projection neurons and were consistent
255 with fate mapping of *hs599*⁺ and *hs953*⁺ cells to projection neuron populations in the
256 adult forebrain, including striatal medium spiny neurons (McGregor et al., 2019;
257 Silberberg et al., 2016) and *Sp8*⁺ neurons in the amygdala (Silberberg et al., 2016).
258 MGE MZ-associated enhancers *hs192* and *hs799* also exhibited markers of early

259 neuronal fate commitment (Figure 3D, Table S4). CI-0, composed predominantly of
260 *hs799*⁺ cells, expressed early MGE-derived cortical interneuron lineage markers
261 including *Maf*, *Mafb*, *Nxph1*, *Calb1*, and *Sst*. Conversely, ci-6, composed of primarily
262 *hs192*⁺ cells, expressed a wide range of TFs including *Tle4* and *Zic1*, *Zic3*, and *Zic4*,
263 suggestive of GABAergic and cholinergic projection neuron commitment (Chen et al.,
264 2010).

265

266 These experiments captured the cell-type specific activity of seven evolutionarily
267 conserved enhancers across E11.5 GEs, showing the feasibility of enhancer-based
268 genetic labeling paired with single cell transcriptomics and resolving lineage and spatial
269 relationships via enhancer labeling. We found regionally separated but otherwise similar
270 mitotic identities among enhancer-labeled progenitors across MGE, LGE, and CGE, and
271 localized regional signatures within MGE via comparing dorsal (*hs1538*⁺) with more
272 ventral *hs1056*⁺ cells. Across GEs, enhancer-labeled neuronal cell types emerged from
273 more general early postmitotic clusters. Postmitotic cells in MGE separated into
274 signatures suggesting GABAergic projection, cholinergic, and interneuron lineages
275 differentially labeled by *hs192* and *hs799*. This initial survey defined specific cell
276 populations and identified known and novel markers for maturation state and regional
277 identity for progenitor and early born neuronal cell types, but had limited resolution to
278 capture heterogeneity within enhancer-labeled cells or profile enhancer-labeled
279 populations against all other cell types.

280

281 **Dissection of early born neuron types and positional identity in MGE via**
282 **enhancer-labeled 3' scRNA-seq and ISH**

283

284 To more deeply interrogate emerging neuronal types labeled by *hs192* and *hs799* in
285 E11.5 MGE, we performed scRNA-seq using the 10x Genomics Chromium system. Our
286 initial scRNA-seq analysis of cells labeled by *hs192* and *hs799* suggested heterogeneity
287 within these labeled early neuronal populations in the MGE. Indeed, fate-mapping
288 experiments for these two enhancers (Silberberg et al., 2016) labeled other, MGE-
289 derived GABAergic, cholinergic, and interneuron populations as well as early born CINs,
290 populations that have not been the focus of previous scRNA-seq studies. FACS-purified
291 MGE ungated and reporter-positive cells were dissected from embryos across three
292 litters for each transgenic line and prepared for multiplexed scRNA-seq using MULTI-
293 seq (McGinnis et al., 2019) (Figure 4A, Table S1). After quality control (Figure S5A-B),
294 4,001 single cells were used for downstream analysis. We used the same TF-curated
295 approach developed for the C1 scRNA-seq dataset to drive cell clustering. Of the 463
296 TFs detected in 10x scRNA-seq MGE data, 421 (90.9%) were represented in both
297 Fluidigm C1 and 10x Chromium systems (Figure 4B, S4F-I). We identified 18 cell
298 clusters in the 10x dataset (Figure 4C). The largest determinant of transcriptional
299 variation across cells was proliferative state (Figure 4D). Consistent with the C1 data,
300 using TFs to drive cell clustering improved performance relative to highly variable gene
301 approaches (Figure S5C-E). Overall, the 10x and MGE-derived C1 data had similar
302 cluster topology and identified similar cell states, as determined by canonical correlation
303 analysis of both datasets (Figure S6).

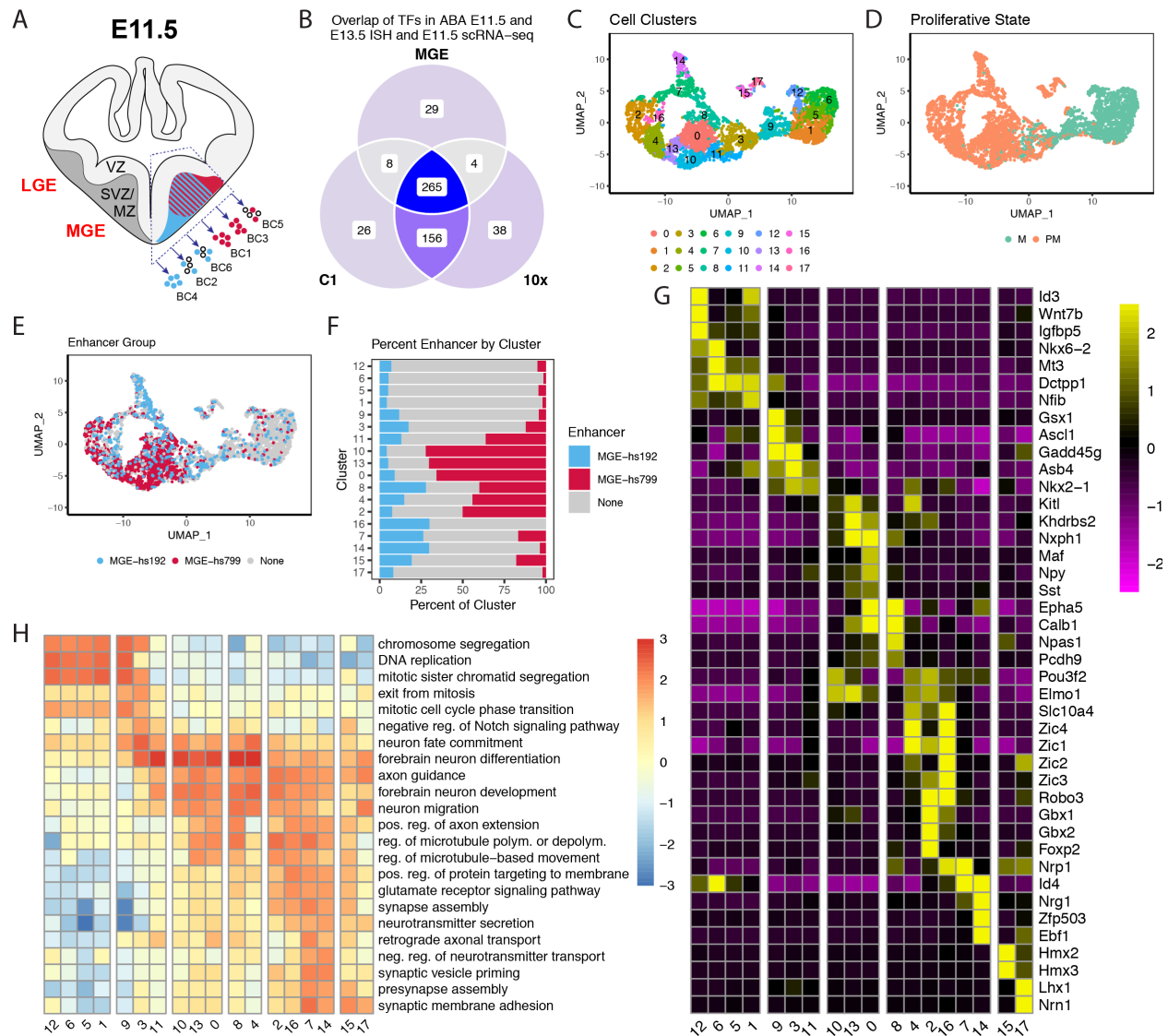


Figure 4: Regional and proliferative gradients within E11.5 MGE.

(A) Schematic of dissections used for MULTI-seq (McGinnis et al., 2019), with colors corresponding to enhancer transgenic reporter expression in the medial ganglionic eminence (red: *hs799*; blue: *hs192*; open circles: unlabeled). LGE: lateral ganglionic eminence; MGE: medial ganglionic eminence; VZ: ventricular zone; SVZ: subventricular zone; BC: barcode. (B) Venn diagram depicting overlap of transcription factors scored within the Allen Developing Mouse Brain Atlas (ABA) for expression in E11.5 or E13.5 basal ganglia and transcription factors detected in 10x and C1 scRNA-seq datasets. (C) UMAP colored by TF-anchored cell clusters. (D) Visualization of single cells from E11.5 MGE by UMAP, colored by mitotic state (green: M, mitotic; orange: PM, postmitotic). (E) UMAP colored by enhancer (red: *hs799*; blue: *hs192*; grey: enhancer-negative). (F) Proportion representation of *hs192*, *hs799*, and enhancer-negative by cluster. (G) Representative differentially expressed genes by cluster. Color represents the mean Z-score of normalized expression across clusters. (H) Representative gene ontology biological process terms separating clusters. Color represents $\log_2(\text{observed/expected})$ for each term.

305 Cells were defined as enhancer-positive for *hs192* or *hs799* if they had at least one UMI
306 (unique molecular identifier) count for CreER^{T2}-IRES-GFP. Enhancer-positive cells from
307 independent samples clustered together, demonstrating reproducibility across biological
308 replicates and distinct distributions of enhancer-labeled *hs192* versus *hs799* cells
309 (Figure 4E). The majority of enhancer-labeled cells mapped to post-mitotic clusters.
310 *hs799*⁺ cells were substantially enriched (>50% of cluster composition) in cl-0, 10, and
311 13, and to a lesser extent in cl-2, 4, 8, and 11 (Figure 4F). In contrast, *hs192*⁺ cells were
312 more broadly distributed, with the greatest representation in postmitotic clusters cl-7, 8,
313 14, 15, and 16, and decreased representation in cl-0, 2, 10, and 13 (Figure 4F). Cells
314 labeled by at least one of the two enhancers were present in all postmitotic clusters
315 alongside ungated enhancer negative cells.

316

317 We next performed differential gene expression (DE) analysis and Gene Ontology
318 analysis across clusters using the full transcriptome of 18,088 genes to identify markers
319 for each cluster and resolve maturation states and cell type identities (Figure 4G-H,
320 Tables S3, S5). Proliferative clusters (cl-1, 5, 6, and 12), corresponding to cells within
321 the MGE VZ, were enriched in terms including 'DNA replication' and 'chromosome
322 segregation' (Figure 4H). In comparison, proliferative clusters cl-9 and cl-3, likely
323 corresponding to cells within the SVZ, were enriched for terms such as 'exit from
324 mitosis' (Figure 4H). Single cell resolution captured initiation of enhancer activity, which
325 is first evident for both *hs799* and *hs192* among individual cells in late SVZ clusters
326 based on transgene expression (Figures 4D-E). Postmitotic clusters subdivided into
327 MGE-derived maturing GABAergic and cholinergic neuron and interneuron lineages (cl-

328 0, 2, 4, 7, 8, 10, 11, 13, and 16), which are differentially labeled by *hs192* and *hs799*,
329 and are described in detail below.

330

331 Some clusters were made up of postmitotic cells that appeared to originate outside the
332 MGE (cl-14, 15, and 17), and were likely migrating through the MGE at E11.5 or
333 captured at dissection boundaries. Cl-14 cells were enriched for *hs192*⁺ cells and had
334 properties of LGE-derived immature medium spiny neurons, which express *Ebf1*, *Nrg1*
335 and *Zfp503 (Nolz1)*, but not *Nkx2-1* (Figure 4G). Cl-15 contained both *hs192*⁺ and
336 *hs799*⁺ cells and may derive from preoptic area (POA), based on *Hmx2 (Nkx5-2)* and
337 *Hmx3 (Nkx5-1)* expression. Cl-17 cells were mostly transgene-negative, and may
338 originate from regions adjacent to the subpallium, e.g. from the hypothalamus or
339 prethalamic eminence. These non-MGE clusters are not further discussed.

340

341 **Projecting scRNA-seq cell identities onto developing mouse MGE via ISH data**

342

343 Using transcriptional cell identities defined by scRNA-seq, we applied ABA ISH
344 expression data (Lein et al., 2007) from the 689 TFs to map the anatomical distribution
345 of cell populations in the E11.5 telencephalon. First, we manually graded expression of
346 curated TFs in the VZ, SVZ, and MZ of MGE and/or LGE by reviewing individual
347 sections from E11.5 and E13.5 in the ABA (Table S2). From this analysis we identified
348 332 genes with visually detectable mRNA ISH patterns in the BG, of which 283 were
349 also detected in E11.5 scRNA-seq from C1 and 10x (Figure S4C). Following
350 comprehensive review of genes with differential scRNA-seq expression and ABA ISH

351 expression patterns in E11.5, E13.5, and E15.5 BG, we identified sentinel genes that
352 could be used as spatiotemporal markers to presumptively assign cells or clusters to
353 distinct neuroanatomical regions and/or specific neuronal lineages on the basis of their
354 mRNA expression profiles. Using these sentinel markers and our scRNA-seq data, we
355 characterized emergent cell lineages and regional distributions of proliferative (Figure 5)
356 and postmitotic (Figure 6) cell populations in the MGE.

357

358 **MGE progenitors stratify by VZ to SVZ and dorsoventral and rostrocaudal axes**

359

360 The analysis of mitotically active cells (*Mki67*⁺; Figure 5A) in the developing MGE
361 provided evidence for distinct progenitor stages and regional patterning (Figure 5B-C).
362 In our analysis, the assignment of four mitotic clusters was driven by genes previously
363 associated with progenitor cell maturation steps, suggesting four discrete histogenetic
364 stages: VZ1 (neuroepithelium), VZ2 (radial glial), SVZ1 (secondary progenitor 1), and
365 SVZ2 (secondary progenitor 2) (Figure 5A). This interpretation is supported by mRNA
366 ISH and scRNA-seq analyses, as described below.

367

368 The most immature VZ stage, the neuroepithelium (VZ1), was represented by cells with
369 the highest expression of early mitotic markers such as *Hes1* and *Id4* (Kageyama et al.,
370 2008) and roughly fit within cl-5 and cl-6 (Figures 5D, S7A). More mature VZ cells (VZ2;
371 perhaps radial glia), organized as a diagonal zone in the UMAP plot, were characterized
372 by expression of *Wnt7b*, *Id3*, and *Ttyh1*; they were roughly contained within cl-12 and
373 the left part of cl-1 (Figures 5E, S7F,G). This zone also had high expression of *Hes5*

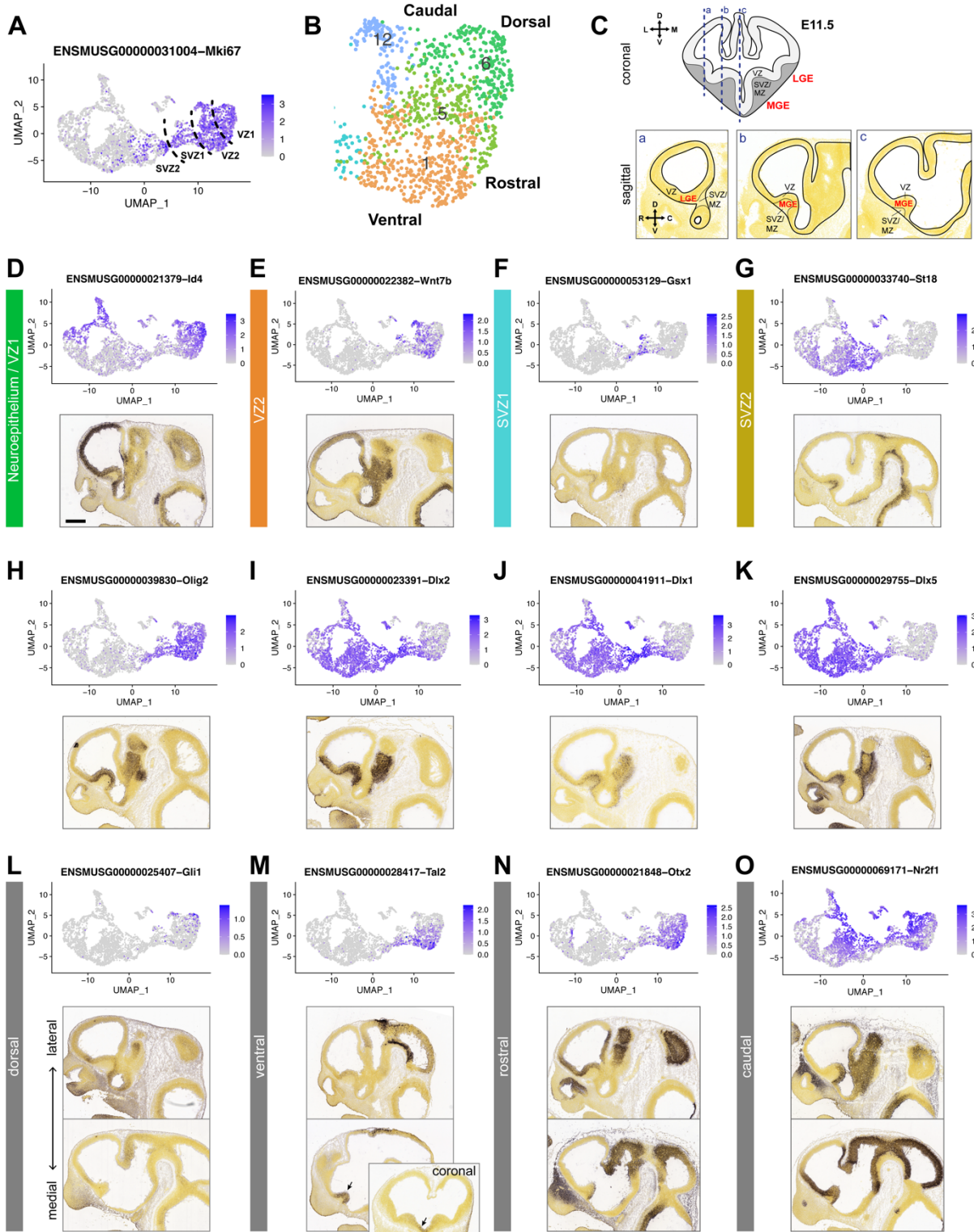


Figure 5: Separation of mitotic progenitors in E11.5 MGE.

(A) Visualization of single cells from E11.5 MGE by UMAP, colored by expression of the mitotic marker *Mki67*. Dotted lines show proposed boundaries for cells from VZ1, VZ2, SVZ1 and SVZ2. (B) Region of UMAP covering the VZ cells, colored by TF-defined cell cluster to show proposed regional identities (also shown in **Figure 4E**). (C) Top: coronal schematic showing the positions (blue dotted lines) of parasagittal sections used to illustrate regional gene expression patterns. Bottom: reference images of parasagittal sections from the ABA with the relevant subpallial anatomical domains labeled. (D-O) Gene expression UMAPs and representative ISH on E11.5 medial parasagittal sections from the ABA showing expression domains for markers of various mitotic cell identities. (D-G) Gene markers for VZ-SVZ developmental stages (*Id4*, *Wnt7b*, *Gsx1*, *St18*). Colored labels correspond to main cell cluster identity for those cells. (H-K) UMAPs and ISH for *Olig2* and *Dlx2/1/5*, genes that help define SVZ1 and SVZ2 identity. (L-O) Gene markers with known regional expression patterns (*Gli1*, *Tal2*, *Otx2*, *Nr2f1*) in the MGE VZ correlate with spatially defined UMAP locations, corresponding to the schematic in (C). Later and medial sections are shown. (M) *Tal2* expression is highest at the medial level; coronal inset shows that this corresponds to the ventral MGE (arrow). Additional genes marking these developmental stages and regional identities are shown in Figures S7-8. Scale bar: 500 μ m.

375 and *Fabp7*, which mark radial glia (Feng et al., 1994; Kageyama et al., 2008) (Figure
376 S7E,H). Other genes strongly marked both VZ zones (Eisenstat et al., 1999; Petryniak
377 et al., 2007; Roychoudhury et al., 2020), including *Lhx2*, *Rest*, and *Rgcc* (Figure S7B-
378 D). Genes like *Ascl1*, *Gsx2* and *Dlx2* began expression in the VZ as scattered cells both
379 in the UMAP plot and by ISH (Figures 5I; S7J,K).
380
381 SVZ organized into the progressively more mature SVZ1 in cl-9 and SVZ2 in cl-3. We
382 assigned SVZ1 identity to cl-9, based on overlapping *Olig2* and *Dlx2* expression
383 (Petryniak et al., 2007) (Figure 5H,I). *Gsx1* showed perhaps the most specific SVZ1
384 periventricular expression by ISH and was largely confined to cl-9 (Figure 5F). Cells in
385 this 'isthmus' cluster also expressed high levels of known SVZ genes (*Ascl1*, *Gsx2* and
386 *Hes6*) (Long et al., 2009; Porteus et al., 1994; Roychoudhury et al., 2020) and
387 neurogenic transition markers (*Btg2*) (Haubensak et al., 2004) (Figure S7J-L).
388 *Gadd45g*, a marker of intermediate progenitors in the cortex (Yuzwa et al., 2017), was
389 also highest in cl-9. SVZ2 identity was linked to cl-3. This most mature progenitor state
390 was associated with the loss of *Olig2* and high levels of *Dlx1*, *2*, and *5* (Eisenstat et al.,

391 1999; Petryniak et al., 2007) (Figure 5H-K). By ISH, cl-3/SVZ2 markers (e.g. *Prox1*, *Sp9*
392 and *St18*) were expressed in a distinct layer of cells superficial to the SVZ1 markers
393 (Figures 5G, S7M,N). *Insm1* and *Isl1* appeared to be expressed in both SVZ1 and SVZ2
394 (Figure S7O,P). Cl-8 and cl-11 may represent the earliest stage of neuronal
395 commitment as SVZ2 cells exit the cell cycle; these clusters are discussed further
396 below.

397

398 Leveraging canonical correlation analysis of MGE cells across both C1 and 10x
399 datasets and ISH data, we found transcription factors and other markers that
400 distinguished the regionally distinct *hs1538* and *hs1056* populations (Figure S6).
401 Markers expressed in cells at the top of the UMAP plot (e.g. *Nkx6-2*, *Gli1* and *Gli2*)
402 indicated dorsal MGE identity (Figures 5L, S8A,B). *Dach2*, a novel marker in this
403 category, occupied a similar location in the UMAP plot and was expressed in the dMGE
404 by ISH (Figure S8C). In the lower part of the UMAP plot, the genes expressed (*Shh*,
405 *Slit2* and *Tal2*) indicated ventral (v)MGE identity (Hoch et al., 2015b) (Figures 5M, S8D-
406 E). The highest expression of vMGE genes was observed in medial sagittal planes of
407 ISH sections (Figure S8D-E). *Bcan*, *Dach1* and *Sulf1* may also mark vMGE progenitor
408 identity (Figure S8F-H). Molecular markers of MGE rostrocaudal position were also
409 identified in the UMAP plot. The rostral MGE had high *Otx2* expression (Hoch et al.,
410 2015b) whereas the caudal MGE was marked by high *Nr2f1* and *Nr2f2* expression (Hu
411 et al., 2017) (Figures 5N,O, S8M). The preoptic area (POA) and pre-optic hypothalamus
412 (POH) are contiguous with the caudal mitotic zone in the MGE. Cl-12 may represent a
413 mixture of POA2 and POH progenitors, based on expression of *Nkx6-2*, *Dbx1*, and

414 *Pax6* (Flames et al., 2007) (Figures S8B,O,P). POA1 cells lack these markers and have
415 higher expression of *Etv1* (Flames et al., 2007); these cells may be intermixed with
416 MGE cells within cl-1. The septum is contiguous with the rostral MGE, and the septal
417 markers *Fgf15* (Borello et al., 2008), *Zic1* and *Zic4* (Inoue et al., 2007; Rubin et al.,
418 2010) were also expressed by rostral MGE progenitors (Figure S8I,J). *Pou3f1* and
419 *Cntnap2* were novel markers of rostral cells (Figure S8K,L), whereas *Ptx3* was a new
420 caudal MGE marker (Figure S8N). These patterning markers, including *Id4*, *Otx2*, and
421 *Tcf7l2*, also distinguished *hs1538* (rostradorsal biased) and *hs1056* (caudoventral
422 biased) cells (Table S4), validating the regional identity evident among MGE
423 progenitors. Thus, this enhancer labeling and TF-curated approach identified TF
424 expression gradients capturing early MGE regional patterning among progenitors.

425

426 **Emergence of MGE neuronal lineages revealed by differential enhancer labeling**

427

428 Postmitotic clusters were identified as the precursors of distinct MGE-derived cell
429 lineages: GABAergic interneurons destined for the cortex (CINs) or other structures,
430 GABAergic projection neurons, and cholinergic neurons (Figure 6A). Importantly, some
431 of these cell types appeared to emerge in different spatial subdomains of the MGE
432 based on marker gene expression. Early-born neurons emerge in SVZ2 and make up
433 the MZ, which can be further visualized via a topological projection map which
434 preserves spatial relationships across the telencephalon (Puelles et al., 2016;
435 Silberberg et al., 2016) (Figure 6B-C). The organization and cellular outputs of the basal
436 ganglia primordia identified herein using this topological map of E11.5 telencephalon

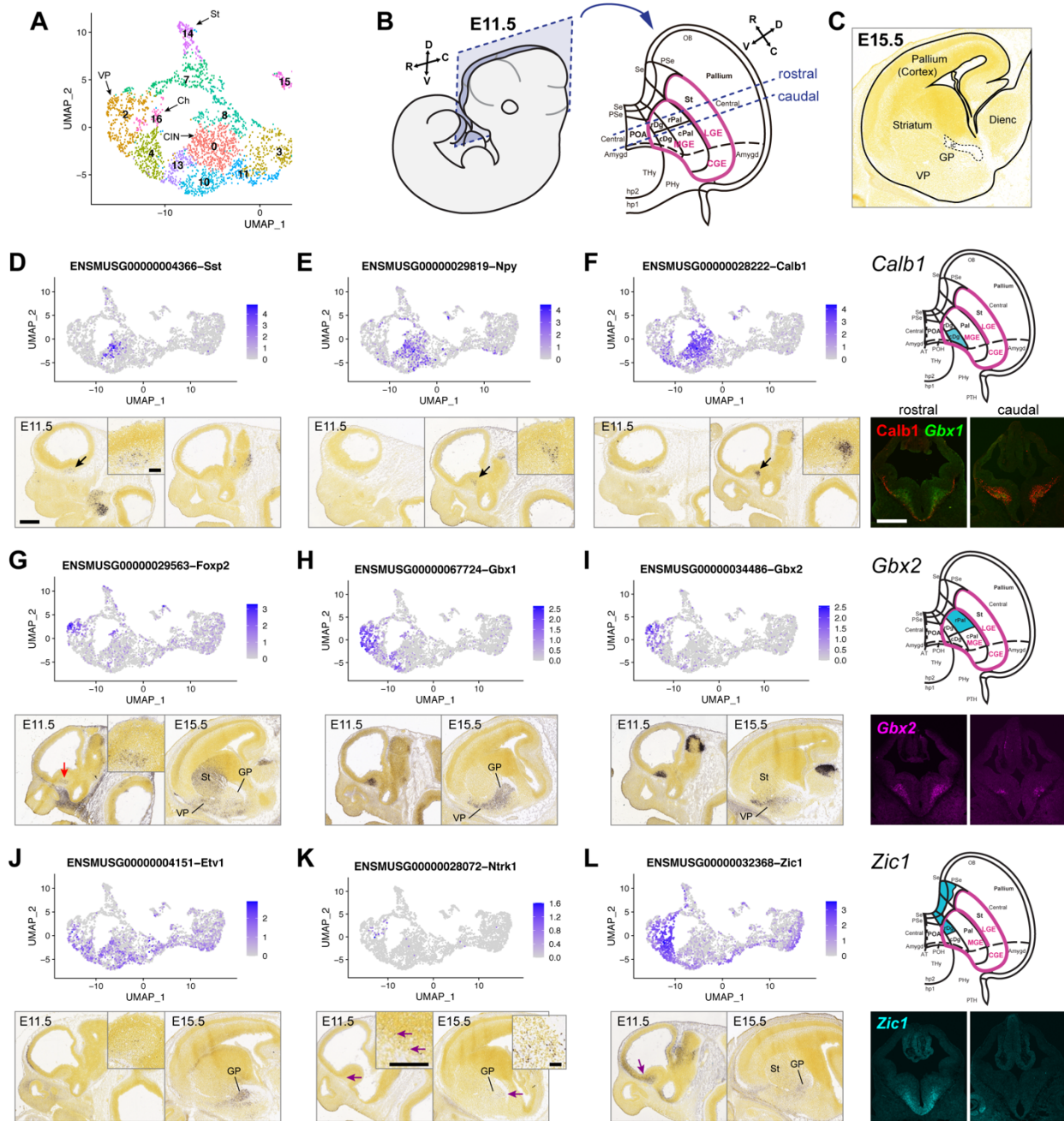


Figure 6: Separation of early neuronal lineages in E11.5 MGE.

(A) Portion of UMAP colored by TF-defined cell cluster (also shown in **Figure 4E**) covering postmitotic cells, with proposed identities of cell clusters labeled. Abbreviations: VP, ventral pallidum; CIN, cortical interneurons; St, striatal medium spiny neurons; GP, globus pallidus; Amygd, amygdala; Ch, cholinergic. (B) Collapsed 2D topological map of the E11.5 MZ, as viewed from the sagittal section plane indicated. The schema is a variant of that in Silberberg et al., 2016. Note the addition of rostral and caudal Pal (Pallidum) and Dg (Diagonal area). See Table S6 for abbreviations. Blue dotted lines (rostral and caudal) indicate positions of coronal fluorescent images shown in **F**, **I** and **L**. (C) Schematic depicting broad anatomical domains at E15.5. VP: ventral pallidum; GP: globus pallidus; Dienc: diencephalon. (D-L) Gene expression UMAPs and representative ISH on E11.5 parasagittal sections from the ABA showing expression of markers for distinct postmitotic neuronal lineages. Arrows indicate regions of higher

magnification insets and cells of interest. Arrow colors: black, CINs; red, VP; purple; Ch. For *Calb1*, *Gbx2* and *Zic1*, a topological schematic illustrates the MZ expression domain for each gene, and coronal sections of fluorescent IHC (*Calb1*) or ISH (*Gbx1*, *Gbx2*, *Zic1*) are also shown to illustrate different MZ expression domains. Scale bars: low magnification, 500 μm ; high magnification insets, 100 μm .

438 correlate with progenitor zone anatomical map of (Flames et al., 2007) (Table S6).
439 Previous scRNA-seq studies have captured some of these emergent neuronal identities
440 but largely have not resolved the spatial organization underlying this process (Mayer et
441 al., 2018; Mi et al., 2018). *Nkx2-1*, *Lhx6*, and *Lhx8* marked the MGE-derived postmitotic
442 neurons (Figure 4G), and these cell groups were further resolved in UMAP plots and
443 cluster assignments by their maturity state and presumed lineage. To analyze these
444 relationships, we focused on major emergent interneuron, GABAergic projection
445 neuron, and cholinergic lineages and the differential activity of *hs192* and *hs799* that
446 distinguishes these specific emerging neuronal populations.
447
448 Cluster cl-0 and a subset of cl-13 were composed primarily of *hs799*⁺ and *hs192*⁻ cells
449 and expressed immature interneuron markers. A subset of cl-8 included *hs799*⁺ and
450 *hs192*⁺ that expressed *Mafb*. Cl-0 showed the most consistent expression of immature
451 CIN markers including *Calb1*, *Cux2*, *ErbB4*, *Lmo3*, *Maf*, *Npy*, *Sox6*, *Sst* and *Zeb2*
452 (Figures 4G, 6D-F, S9A-G). Earlier lineage markers such as *Lhx8* were reduced in
453 these cells. Subsets of cl-13 and cl-8 cells were *Mafb*⁺, but lack *Maf* and other CIN
454 markers. The small proportion of *Maf*⁺ *hs192*⁺ cells in cl-8 and cl-0 was consistent with
455 our C1 data and in line with fate mapping of a subset of *hs192*-lineage cells to CINs
456 (Silberberg et al., 2016). Sentinel genes for cells from cl-0 and cl-13 were expressed in
457 a distinct area in the periventricular mantle zone of the caudal MGE based on ISH at
458 E11.5. We found that *Calb1* expression is largely located in the caudal Diagonal (Dg)

459 region, as illustrated on the topological map of the telencephalon (Figure 6F). The
460 caudal Dg also showed expression of *Cux2*, *ErbB4*, *Npy*, *Sst*, *Maf*, and *Mafb*; the latter
461 two genes are perhaps the most specific markers of MGE-derived CINs (Mckinsey et
462 al., 2013; Pai et al., 2019) (Figure 6D,E, S9A-D). Contiguous with this region, in more
463 lateral ISH sections, were cells expressing CIN markers, presumably migrating to the
464 LGE and/or CGE on their way to the cortex (e.g. *Sst* and *Calb1* in Figure 6D,F).
465 Additionally, *Adamts5*, *Bend4*, *Dlgap1*, *Kitl* and *Rai2* may be novel markers of immature
466 CINs (Figures S9H,I). Based on putative maturation states and overlapping
467 transcriptional signatures, immature interneurons from these three clusters can be
468 presumptively mapped back to late progenitor cells in SVZ2 (cl-3) via cl-11 for cl-0, cl-10
469 to cl-11 for cl-13, and within cl-8. These findings map the neurogenic progression and
470 distinct spatial niches for emerging early MGE-derived interneurons, including *hs799*⁺
471 cells that contribute to SST⁺ CINs, as well as other populations.

472

473 Of particular interest, the scRNA-seq signatures and corresponding ISH patterns
474 suggested at least two distinct classes of GABAergic projection neurons differentially
475 labeled by *hs799* and *hs192* and distinguished by *Gbx1*⁺ or *Zic1*⁺ expression,
476 respectively, that originate in different parts of the MGE (Figure 6H,L). The first
477 GABAergic projection class was preferentially labeled by *hs799* and expressed *Gbx1*,
478 with more restricted expression of *Foxp2* and *Gbx2*, and corresponded to *Shh*⁺ cl-13
479 cells and to subsets of cl-4 and cl-2 (Figures 6G-I, S8D). Based on a distribution on the
480 UMAP, *Gbx1*, *Kitl*, *Lmo3*, *Sox6*, *Th*, *Tle4*, *Tshz2*, *Zeb2* and *Zic1* (Flandin et al., 2010;
481 Mckinsey et al., 2013) are additional markers for cells from cl-2, cl-4, and cl-13 (Figures

482 4G, 6L, 7D, S9E-H,J,K). These cells were presumptively mapped to less mature states
483 in cl-10 and cl-1 (for cl-13 only) or cl-4 and cl-11 (for cl-2). On the topological map of the
484 MGE, *Gbx2* expression was in the rostral portion of the pallidal (Pal) subdivision (Figure
485 6I). Anatomically, the E15.5 expression domains of *Foxp2*, *Gbx2*, *Gbx1* and *Etv1*,
486 determined by ISH, were nested along the pallidum's radial axis. *Foxp2* expression was
487 largely superficial, possibly in the ventral pallidum (Campbell et al., 2009) (Figure 6G).
488 *Gbx1* expression encompassed the ventral pallidum and the entire globus pallidus
489 (Figure 6H). *Gbx2* included the ventral pallidum and part of the globus pallidus (Chen et
490 al., 2010) (Figure 6I). *Etv1* was expressed throughout the globus pallidus but in few
491 cells in the ventral pallidum (Flandin et al., 2010) (Figure 6J). *Foxp2*⁺ cells become
492 superficial pallidal projection neurons (i.e. ventral pallidum), whereas other cl-2 cells,
493 and some cl-4 and cl-13 cells, contribute to deeper pallidal structures (i.e. globus
494 pallidus). Thus, we propose these populations that share increased *hs799* activity
495 branch from immature neuron types within cl-2, cl-4, and cl-13.

496
497 The second GABAergic lineage expressed *Zic1*, as well as more restricted expression
498 of *Zic3* and *Zic4*, and was enriched for cells with high *hs192* activity (Figure 6L). *Zic* TFs
499 ISH MGE expression was restricted to the rostroventral MGE and overlapped little with
500 *Gbx2*; *Zic1* may not overlap with the more caudal CIN markers (Figure 6D-F; S10A-D).
501 On the topological map, *Zic1* expression was restricted to the rostral Dg region, and
502 was continuous with *Zic1* expression in the septum (Figure 6L). As noted, *Zic1* was also
503 expressed in the VZ and SVZ of the rostral MGE and septum, suggesting that this
504 progenitor zone generates the *Zic1*⁺ postmitotic cells in cl-11 and cl-4. It is unclear from

505 ISH how *Zic1*-associated GABAergic projection neurons are spatially organized within
506 the GP, though the spatial organization appears more diffuse across the GP. These
507 *hs192*-biased *Zic1*⁺ cells may constitute a distinct cell type within the GP.
508
509 Cells in cl-16 were exclusively enhancer *hs192*⁺ and *hs799*⁻ and expressed definitive
510 cholinergic marker genes. Among these, *Ntrk1* (Sanchez-Ortiz et al., 2012) was the
511 most specific to this cluster (Figure 6K). Although *Ntrk1* expression was weak in ISH at
512 E11.5, scattered positive cells were visible in the striatum and GP by E15.5, consistent
513 with the distribution of cholinergic interneurons (Figure 6K). Cl-16 cells also expressed
514 *Gbx1*, *Gbx2*, *Isl1* and *Zic4*, all of which are cholinergic lineage markers (Fragkouli et al.,
515 2009; Chen et al., 2010; Magno et al., 2017; Asbreuk et al., 2002; Elshatory and Gan,
516 2008), as well as *Zic1*, *Zic2*, and *Zic5* (Figures 6H,I,L, S9L,M). *Fgf15* appeared to be a
517 novel marker of this population, but its expression was not maintained as cells mature
518 (Figure S9N). A subset of *hs192*⁺ cl-4 cells also expressed some of these markers (e.g.
519 *Zic2*) and may represent a less mature state or another type of cholinergic neuron. *Fgf8*,
520 *Fgf17*, and *Nkx2-1/Zic4* fate mapping provides evidence that these cells arise from the
521 junction of the rostromedioventral MGE with the septum (Magno et al., 2017; Hoch et
522 al., 2015a), consistent with the expression of *Zic1*.
523
524 The final postmitotic group, cl-7, included two populations: the upper part was almost
525 exclusively *hs192*⁺, while the lower part also contained *hs799*⁺ cells. The upper part of
526 cl-7 was *Nkx2-1*⁻ and strongly expressed *Six3* and *Sp8* (Figure S9O,P), suggesting a
527 CGE-derived CIN or LGE-derived olfactory bulb IN identity (Long et al., 2007). The

528 lower part of cl-7 was *Nkx2-1*⁺ and *Lhx8*⁺ (and thus likely MGE-derived); these cells also
529 expressed genes shared by cl-2 and cl-14, including *Id4* and *Tle4* (Figures 5D, 7D).
530 Earlier states of cl-7 cells appeared to map back to cl-8 then SVZ2 cl-3 cells, with *Nr2f2*
531 expression in these clusters indicating caudal MGE origin (Figure S8M).

532

533 Across described postmitotic populations, enhancer-labeled scRNA-seq and ABA ISH
534 indicated specific spatial localizations for cell types with divergent transcriptomic
535 identities. To verify this finding, we performed fluorescent immunohistochemistry (IHC)
536 and ISH to map protein expression across coronal sections for four sentinel genes
537 representative of these populations (Figure 6F,I,L). We examined *Calb1* for early CINs,
538 predicted to be located in caudal Dg; *Gbx1* and *Gbx2* for GABAergic projection neurons
539 in rostral Pal; and *Zic1* for rostral Dg GABAergic projection and cholinergic populations.
540 These experiments validated that early born neuronal populations indeed exhibit spatial
541 segregation to specific rostrocaudal and dorsoventral zones of the MGE MZ. Thus, our
542 experiments captured novel lineage progression and associations between spatial and
543 transcriptomic identity of E11.5 MGE-derived neuron populations.

544

545 **Validation of MGE enhancer-labeled progenitor and postmitotic populations**

546

547 The combination of enhancer labeling and scRNA-seq paired with ISH defined distinct
548 populations marked by progenitor (*hs1538* and *hs1056*) and postmitotic (*hs192* and
549 *hs799*) enhancers in the MGE. We used ISH and co-labeling to validate transcripts that
550 distinguish cells between these postmitotic and mitotic enhancer pairs. We found subtle

551 but detectable transcriptomic differences between MGE progenitor cells labeled by
552 *hs1538* and *hs1056* corresponding to regional spatial segregation of *hs1538* to dMGE
553 VZ and *hs1056* to vMGE (Table S4). In contrast, there were broad transcriptional
554 differences between the spatially intermixed populations of postmitotic cells labeled by
555 *hs192* and *hs799* in the MGE (Tables S3,S4, Figures 3,5). Between *hs1538* and
556 *hs1056*, among the most informative transcripts for differential enhancer labeling were
557 *Id4*, *Tcf7l2*, *Zkscan1*, *Otx2*, and *Satb1* (Table S4). While the differential scRNA-seq
558 signatures were subtle, ISH verified highest expression of the *hs1538*-associated
559 marker *Id4* in the VZ of the dorsal and rostral MGE where *hs1538* is active (Figure 7A).
560
561 In postmitotic populations, *hs192* activity, which was biased toward GABAergic
562 projection neurons in the striatum and cholinergic interneurons, was associated with
563 higher levels of the transcription factor *Tle4* and several members of the *Zic* TF family
564 including *Zic1*, *Zic3*, and *Zic4* (Table S4). Conversely, *hs799* activity favored
565 populations of early CIN lineages expressing markers including *Mafb* and *Sst*, in
566 addition to its activity in GABAergic projection neurons. As *hs192* and *hs799* MZ
567 populations spatially intermingle, ISH alone was insufficient to verify specificity. Thus, to
568 validate differential expression of genes across *hs192* and *hs799* labeled cells, we
569 performed co-labeling of GFP⁺ enhancer-labeled cells and *Tle4* and *Zic1*, two
570 transcription factors that were enriched in *hs192*⁺ cells (Figure 7B,C-F). As expected,
571 enhancer-positive cells showed overlapping distributions in the MGE, but *hs192* activity
572 and *Zic1* expression were highest in the rostroventral MGE and paraseptal region
573 (Figure 7C,F). In addition, *Tle4* protein was expressed in significantly more *hs192* GFP⁺

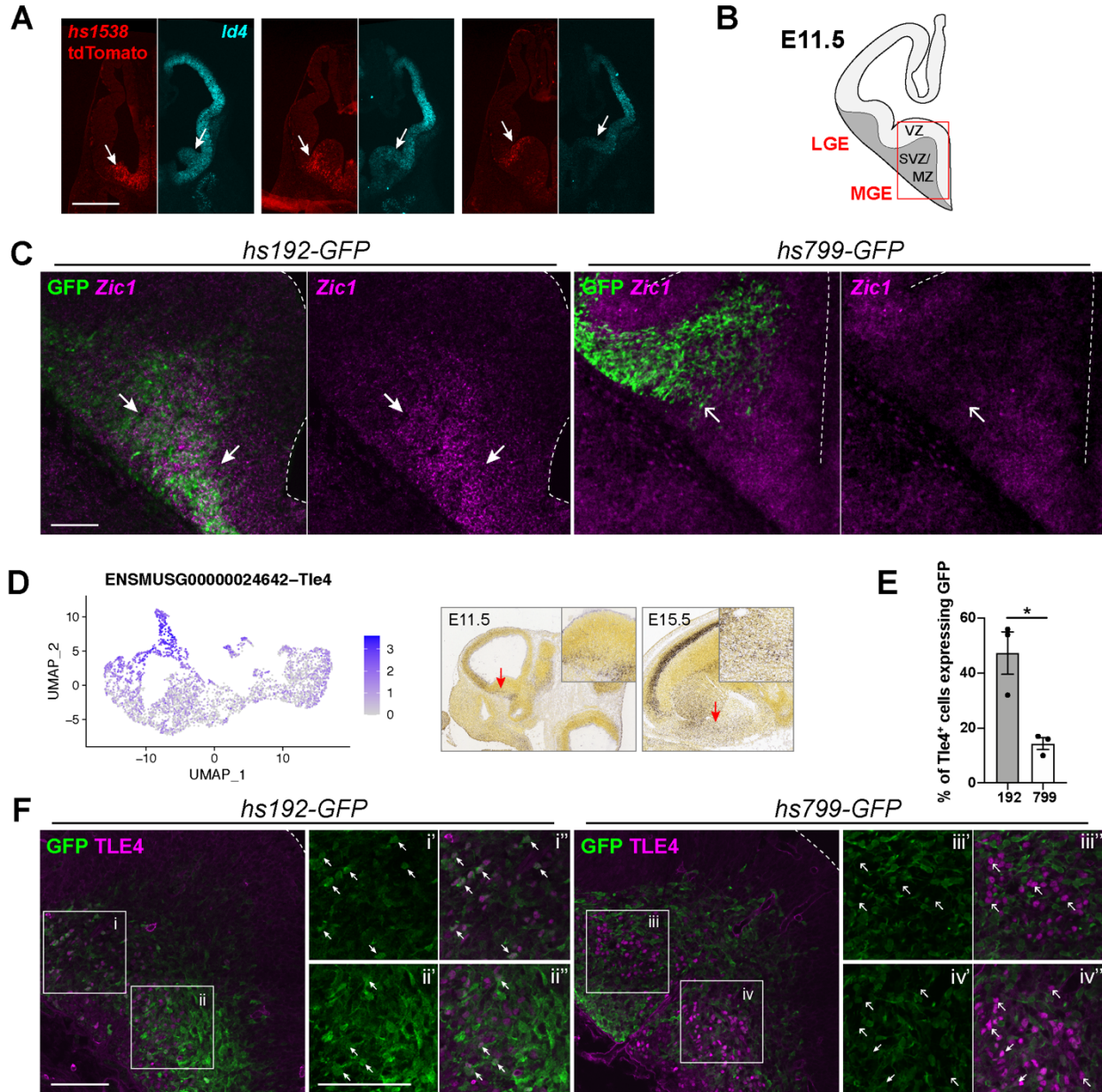


Figure 7: Spatial and epigenomic differences in E11.5 MGE enhancers.

(A) Endogenous tdTomato expression (red) in *hs1538* E11.5 coronal sections after tamoxifen administration at E10.75, and *Id4* fluorescent ISH (cyan) on equivalent wildtype E11.5 sections. Arrows point to higher expression in the rostral and dorsal MGE VZ compared with ventral MGE. Scale bar: 500 μ m. (B) Schematic showing location (red box) of low magnification images shown in (C) and (F). (C) *Zic1* fluorescent ISH (magenta) and GFP immunohistochemistry (green) on superimposed adjacent coronal sections of E11.5 *hs192* and *hs799* forebrain. Closed arrows indicate *hs192* GFP overlaps with *Zic1* expression in the ventral MGE. Open arrows indicate the ventral extent of *hs799* GFP cells, which does not extend into the region of high *Zic1* expression. (D) UMAP of *Tle4* expression and representative ISH on E11.5 sagittal sections from the ABA. (E) Quantification of percent of *Tle4* cells that are also GFP positive from (F). (F) Immunohistochemistry for *Tle4* and GFP on *hs192* and *hs799* coronal sections. Double-positive cells are indicated by closed arrows and GFP-negative cells are indicated by open arrows. Scale bars: 100 μ m. Ventricular surface of MGE is indicated by dotted lines.

575 cells compared to *hs799* GFP⁺ cells (Figure 7E). Thus, ISH and co-labeling experiments
576 validate the results from scRNA-seq-based separation of enhancer-labeled MGE cells.

577

578 **Discussion**

579

580 Transcriptional profiling at single cell resolution has transformed our understanding of
581 the diversity of cell types in the brain. While initial efforts to catalogue brain cell types
582 have returned huge gains (Zeisel et al., 2018), new approaches are now needed to link
583 transcriptional identity to location, function, and developmental lineage. Here, we
584 combined novel enhancer-based cell labeling, TF-anchored clustering, and ISH-based
585 spatial annotation to map the neurogenic landscape of embryonic mouse basal ganglia.
586 Through this integrated approach, we illuminate enhancer activity in specific cells in vivo
587 and provide new insights regarding the specification paths for early GABAergic
588 neurogenesis in the ganglionic eminences.

589

590 Enhancer activity is often tightly restricted to specific cell types and developmental
591 stages (Dunham et al., 2012; Nord, 2013; Reddington et al., 2020), making enhancers
592 potent tools for genetic labeling and manipulation (Pattabiraman et al., 2014; Silberberg
593 et al., 2016; Visel et al., 2013). However, the specificity and pattern of enhancer action
594 in vivo at the single cell level has not been deeply explored. Most studies that examine
595 enhancer specificity in the brain have used image-based assays of reporter expression
596 (Visel et al., 2013) or orthogonal biochemical and epigenomic proxies to predict cell-
597 type specific enhancer activity (Dunham et al., 2012). In contrast, our approach

598 represents a major advance in resolution for in vivo function-based modeling of
599 enhancer activity. Our results demonstrate that scRNA-seq can capture reporter
600 transcripts across histogenetic subtypes labeled by individual enhancers, thus
601 identifying enhancer-positive cells with high specificity even when enhancer activity was
602 low or limited to specific cell types. scRNA-seq analysis revealed the onset and offset of
603 enhancer activity as well as cell populations where each enhancer was active with fine-
604 scale resolution. Overall, this study reinforces the specificity of activity across individual
605 enhancers and increases resolution of enhancer activity mapping to offer a
606 representative perspective of in vivo single cell enhancer activity for seven evolutionarily
607 conserved neurodevelopmental enhancers.

608

609 Numerous genetic studies have probed mechanisms of BG development, with two
610 recent studies (Mayer et al., 2018; Mi et al., 2018) using scRNA-seq to follow BG
611 development and CIN lineage specification in E12.5-E14.5 embryonic mouse. Our
612 results capture an earlier time when alternative neuronal lineages originate, using
613 enhancer labeling, TF curation, and ISH to enable lineage tracking and spatial
614 resolution of progenitor and postmitotic populations across the GEs. Similar to other
615 studies, our results find transcriptomic differences among progenitor and postmitotic
616 cells across the GEs, with additional markers of maturation and postmitotic lineages
617 resolved via enhancer labeling. Further, integrating ISH data, we assigned likely
618 identities to four types of MGE progenitors; distinct MGE progenitor regions; and
619 enhancer-labeled subtypes of maturing MGE-derived interneurons, GABAergic

620 projection neurons, and cholinergic neurons that together mature to form pallidal
621 structures or migrate to become interneurons in the cortex, amygdala, and striatum.
622
623 Progenitor cohorts with overlapping transcriptional states and region-specific signatures
624 were labeled by spatially distinct enhancers with VZ activity (*hs1538*, *hs1056*, *hs841*;
625 Figures 2,3,4). Similar to published studies at older ages (Mayer et al., 2018; Mi et al.,
626 2018), we found at E11.5 that scRNA-seq resolves the maturation gradient of BG
627 progenitor populations from NSCs in the VZ to postmitotic neuronal precursors in SVZ2
628 (Figure 5A). Comparison of *hs1538*⁺ and *hs1056*⁺ enabled the discovery of genes
629 whose expression in MGE progenitors defined rostrocaudal and dorsoventral axes. The
630 rostradorsal *hs1538*⁺ progenitors were enriched for *Id4*, *Otx2*, *Tcf7l2*, and *Zic1* (Figures
631 3, 5, 7; Table S4). In contrast, caudoventral progenitors were enriched for *Nr2f1/2* and
632 *Tal2* (Figure 5). Interestingly, *Id4* is both associated with neuroepithelial progenitors
633 (Bedford et al., 2005; Yun et al., 2004) and biased toward rostradorsal MGE VZ,
634 suggesting potential differences in progenitor state composition across regional
635 domains within E11.5 MGE VZ. Of note, progenitors segregated on the UMAP across
636 these axes when using a TF-anchored transcriptome analysis (Figure 5). We suggest
637 that positional information in E11.5 MGE progenitors is largely encoded by gradients of
638 these and other TFs rather than the expression of specific TF domains. Combinations of
639 TFs then activate region-specific enhancers such as *hs1538*, as has been shown in
640 classic model of ectoderm patterning in drosophila embryos (Levine, 2008) and in the
641 cortical VZ (Pattabiraman et al., 2014).
642

643 Early-born CGE, LGE and MGE GABAergic projection, cholinergic, and inhibitory
644 neuronal lineages are labeled by differential enhancer activities (*hs953*, *hs599*, *hs192*,
645 *hs799*, respectively) (Figures 3,4,6). Compared to the distinct MGE signature, LGE and
646 CGE cells had more similar transcriptomic identities, but diverged between *hs599* and
647 *hs953* cells in later post-mitotic neuron clusters. Focusing on MGE, differential scRNA-
648 seq comparison of enhancers *hs192* and *hs799* in combination with ISH annotation
649 defined three spatially distinct regions in the MGE MZ that give rise to molecularly
650 distinct cells. CINs (expressing multiple markers) were detected in the caudal Diagonal
651 (Dg) region (Figure 6F). *Gbx1/2*⁺ cells were mapped to the Pallidal (Pal) region and
652 *Zic1*⁺ cells to the rostral Dg regions (Figure 6I,L). We are intrigued by the possibility that
653 *Gbx*⁺ and *Zic*⁺ cells contribute to distinct types of MGE GABAergic neurons, including
654 within the GP, in addition to the cholinergic neurons already described (Chen et al.,
655 2010; Magno et al., 2017). Previous studies have not identified a specific MGE region
656 giving rise to CINs, nor spatially distinct zones for the generation of pallidal neurons and
657 CINs. This contrast to our findings may be because our analysis focused on a younger
658 age (E11.5) than most studies. Consistent with our results, (Puelles et al., 2016)
659 previously showed that *Sst* expression begins in the Dg region. It is probable that as
660 development proceeds, additional MGE regions also generate CINs, as suggested by
661 many studies (Mayer et al., 2018; Mi et al., 2018; Silberberg et al., 2016). Overall, the
662 results from these experiments define emerging GABAergic neuron types and elucidate
663 relationships between spatial and transcriptomic characteristics of lineages in
664 embryonic BG and in early mammalian brain development.
665

666 Beyond BG neurogenesis, our study has broader implications for the application of
667 scRNA-seq to developing tissues. We demonstrate that anchoring scRNA-seq analysis
668 on TF transcripts reduces the weight of cell cycle-driven and technical sources of
669 variation (noise), improving the power of histogenetic cell type classification. Limiting
670 analysis to TF transcripts greatly improved resolution of regional identity and maturation
671 state for progenitors in the VZ and SVZ, consistent with the vast body of literature
672 defining TF gradients as the master regulators of lineage specification in the BG and
673 elsewhere. The extensive use of ISH annotations to define regional gradients enabled
674 us to identify and interpret patterns of cell identity captured in scRNA-seq data. Finally,
675 enhancer labeling enabled us to enrich, identify, and compare specific progenitor
676 populations and early neuronal lineages, capturing novel transcriptional signatures for
677 labeled lineages. Our results highlight the value and need for curated approaches in
678 scRNA-seq analysis (e.g. our focus on TF transcripts) and the utility of leveraging
679 orthogonal and accessory data, in this case ISH and enhancer labeling, to understand
680 complex developmental processes. This study thus represents a new frontier, pairing
681 scRNA-seq with functional analysis of enhancer activity in vivo and highlighting the
682 utility of combining enhancer-mediated expression for labeling and characterization of
683 specific cell types and offers insight into GABAergic neurogenesis in the embryonic
684 mouse BG.

685 **ACKNOWLEDGEMENTS**

686 Next-generation sequencing was performed at the Center for Advanced Technology at
687 UC San Francisco and the UC Davis DNA cores. Confocal microscopy was performed
688 at the UC San Francisco Nikon Imaging Center, supported by NIH S10 Shared
689 Instrumentation grant 1S10OD017993-01A1. Cell sorting was performed at the UC San
690 Francisco HDFCC Laboratory for Cell Analysis, using instrumentation supported by NIH
691 grant P30CA082103. Additional cell sorting and C1 scRNA-seq were performed at the
692 UCSF Parnassus Flow Core (RRID:SCR_018206) supported in part by Grant NIH P30
693 DK063720 and by the NIH S10 Instrumentation Grant S10 1S10OD021822-01. 10x
694 scRNA-seq was performed by the UCSF IHG Genomics Core. L.S.-F. was supported by
695 the UC Davis Floyd and Mary Schwall Fellowship in Medical Research, the UC Davis
696 Emmy Werner and Stanley Jacobsen Fellowship, and by grant number T32-GM008799
697 from NIGMS-NIH. R.C.-P. was supported by a Science Without Borders Fellowship from
698 CNPq (Brazil). This work was supported by the following research grants. J.L.R.R.:
699 NIMH R01 MH081880 and NIMH R37/R01 MH049428. A.S.N.: NIH/NIGMS R35
700 GM119831. Z.J.G.: Department of Defense Breast Cancer Research Program
701 (W81XWH-10-1-1023 and W81XWH-13-1-0221), NIH (U01CA199315 and DP2
702 HD080351-01), NSF (MCB-1330864), and the UCSF Center for Cellular Construction
703 (DBI-1548297), an NSF Science and Technology Center. Z.J.G. is a Chan-Zuckerberg
704 BioHub Investigator. L.P. was supported by Seneca Foundation (5672 Fundación
705 Séneca, Autonomous Community of Murcia) Excellency Research contract:
706 19904/GERM/15; project name: Genoarchitectonic Brain Development and Applications
707 to Neurodegenerative Diseases and Cancer.

708

709 **AUTHOR CONTRIBUTIONS**

710 L.S.-F. and A.N.R. are listed as joint first authors, as each led components of the
711 experiments and analysis. J.L.R.R. and A.S.N. are listed as joint senior and
712 corresponding authors. L.S.-F., A.N.R., S.N.S., J.L.R.R., and A.S.N. designed the
713 experiments. Dissections, single-cell preparations and histology: A.N.R. and S.N.S.;
714 scRNA-seq library preparation: L.S.-F., A.N.R., and I.Z.; bioinformatics: L.S.-F., R.C.P.,
715 K.J.L., C.S.M., T.E.R., Jr., and A.S.N.; in situ hybridization prioritization and scoring:
716 S.N.S., G.L.M., M.H., C.T., and H.Z. Topological map: L.P. and J.L.R.R. L.S.F., A.N.R.,
717 J.L.R.R., and A.S.N. drafted the manuscript. All authors contributed to manuscript
718 revisions.

719

720 **DECLARATION OF INTERESTS**

721 J.L.R.R. is cofounder, stockholder, and currently on the scientific board of *Neurona*, a
722 company studying the potential therapeutic use of interneuron transplantation.

723

724

725 **Methods**

726 **RESOURCE AVAILABILITY**

727 **Lead Contact**

728 Further information and requests for resources and reagents should be directed to and
729 will be fulfilled by the Lead Contacts, Alex S. Nord (asnord@ucdavis.edu) and John L.
730 R. Rubenstein (john.rubenstein@ucsf.edu).

731

732 **Materials Availability**

733 The enhancer transgenic mouse lines used in this study have been previously published
734 (Silberberg et al., 2016) and deposited to the MMRRC repository.

735

736 **Data and Code Availability**

737 The datasets generated during this study are available on GEO (accession TBD). The
738 analysis codes used for this study can be found on the Nord Lab Git Repository
739 (<https://github.com/NordNeurogenomicsLab/>).

740

741 **EXPERIMENTAL MODEL AND SUBJECT DETAILS**

742 ***Mice***

743 The enhancer transgenic mouse lines used in this study have been previously published
744 (Silberberg et al., 2016) and deposited to the MMRRC repository. All animal care,
745 procedures, and experiments were conducted in accordance with the NIH guidelines
746 and approved by the University of California, San Francisco animal care committee's
747 regulations (Protocol AN180174-02). Pregnant dams were housed in mating pairs, or

748 singly housed with additional environmental enrichment. Mice were housed in a
749 temperature-controlled environment (22-24°C), had ad libitum access to food and water,
750 and were reared in normal lighting conditions (12-h light-dark cycle). Embryos of either
751 sex were used, and all embryos of the correct genotype from a single litter were pooled
752 as a single biological replicate for all sequencing experiments.

753

754 We used mice from 7 previously published enhancer transgenic lines (Silberberg et al.,
755 2016): *hs192-CreER^{T2}-IRES-GFP*, *hs599-CreER^{T2}-IRES-GFP*, *hs799-CreER^{T2}-IRES-*
756 *GFP*, *hs841-CreER^{T2}-IRES-GFP*, *hs953-CreER^{T2}-IRES-GFP*, *hs1056-CreER^{T2}-IRES-*
757 *GFP* and *hs1538-CreER^{T2}-IRES-GFP*, herein referred to simply by their enhancer ID,
758 e.g., *hs192*. Enhancer line hemizygous transgenic male mice were mated to CD-1
759 wildtype or *Ai14* tdTomato Cre-reporter female mice (MGI ID: 3809524) (Madisen et al.,
760 2010) to obtain embryos for experiments. All transgenic mice were maintained on a
761 mixed background outcrossed to CD-1. For inducible tdTomato labeling of enhancer
762 positive cells with the *hs1538* line, *Ai14* reporter female mice were mated to enhancer
763 transgenic males and dosed with 55 mg/kg tamoxifen dissolved in corn oil at 6 pm the
764 day before embryo harvest (E10.75 for harvest at E11.5). 14 mg/kg progesterone was
765 included to improve embryo survival.

766

767 **METHODS DETAILS**

768 **C1 scRNA-seq**

769 *Cell isolation.*

770 Pregnant dams were sacrificed by CO₂ inhalation, confirmed by cervical dislocation.

771 E11.5 embryos were removed and placed into ice-cold Earle's Balanced saline solution
772 (EBSS). Transgene-positive embryos were identified by screening on a fluorescent
773 microscope. In a clean dish with ice-cold EBSS, the MGEs, LGEs or CGEs were
774 dissected out and placed into a 1.5 mL Eppendorf tube containing EBSS on ice. Tissue
775 was pooled from all transgene-positive embryos in a single litter.

776

777 The tissue was dissociated in 300 µL of 0.25% trypsin-EDTA solution supplemented
778 with 10 U/mL recombinant DNase I (Roche) for 15 minutes at 37°C. Trypsinization was
779 stopped by addition of 300 µL DMEM with 10% FBS, and the tissue was gently
780 triturated 10-15 times with a P1000 pipette and filtered through a 40 µm filter to achieve
781 a single-cell suspension. The cells were spun down for 3 minutes at 500 rcf and
782 resuspended in FACS buffer (EBSS + 0.5% BSA + 2 mM EDTA). DAPI (50 ng/mL final
783 concentration) was included to stain dead cells.

784

785 For gated samples, GFP- and tdTomato-positive cells were isolated by fluorescence
786 activated cell sorting on a FACSAria II flow cytometer (BD Biosciences). FACS gating
787 was set using a transgene-negative sample, and DAPI-positive dead cells were
788 excluded. Single-cell sorting mode was used to maximize sample purity. For ungated
789 samples, DAPI-stained cells were excluded but GFP-positive and GFP-negative cells
790 were collected.

791

792 *C1 cell capture and cDNA generation.*

793 For unsorted and ungated experiments, cells were counted on a haemocytometer and
794 diluted to 150-300 cells/ μ L in FACS buffer. The cell mix was prepared and loaded onto
795 a Fluidigm integrated fluidics chip (C1™ Single-Cell mRNA Seq IFC, 5–10 μ m, #100-
796 5759) on the Fluidigm C1 system according to the manufacturer's instructions.

797

798 For GFP- and tdTomato-gated samples, cells were sorted directly into the loading well
799 of the IFC (integrated fluidic circuit) according to the manufacturer's note

800 (<https://www.fluidigm.com/articles/cell-sorting-directly-to-the-c1-ifc>). Briefly, the IFC

801 plate was placed on the plate chiller of the FACS Aria sorter, the inlets were covered
802 with PCR-plate sealing film, and the sort stream was directed to the cell loading well.

803 The film over the cell loading well was removed and 3 μ L of C1 cell suspension buffer
804 was added to the well. 1,500 cells were then sorted directly into the well. Finally, 1.5 μ L
805 of FACS buffer was added to give a final volume of 7.5 μ L and a concentration of 200
806 cells/ μ L. The cell suspension was pipetted gently 2-3 times to mix, and cells were
807 loaded onto the IFC using the C1 machine according to the manufacturer's instructions.

808 After capture, each well of the IFC was visually examined on a Keyence microscope
809 and scored for the number of cells and presence or absence of cell debris.

810

811 Cell lysis, reverse transcription and cDNA amplification were performed on the Fluidigm
812 C1 machine according to the manufacturer's mRNA-seq protocol using the SMARTer
813 Ultra Low RNA Kit for the Fluidigm C1 System (Takara Bio #634833). cDNA amplicons
814 (~3 μ L) were harvested into a 96-well plate containing 10 μ L C1 DNA dilution buffer per
815 well, as described in the protocol, and stored at -80°C for library preparation.

816

817 *C1 scRNA-seq library preparation.*

818 1 uL of diluted cDNA per well was used for library preparation using the Nextera XT

819 DNA Sample Prep Kit (Illumina, #FC-131-1096). Each C1 IFC was pooled into one

820 library, for a total of up to 96 samples per library. Sequencing library quality was

821 assessed using the high-sensitivity dsDNA assay in an Agilent Bioanalyzer.

822

823 **Multiplexed 10x scRNA-seq library generation (MULTI-seq)**

824 E11.5 MGE tissue was dissected as described above and dissociated using the Papain

825 Dissociation System (Worthington) with a modified protocol. MGEs pooled from a single

826 litter were incubated with 200 μ L papain solution supplemented with 10 U/mL

827 recombinant DNase I (Roche) for 10 minutes at 37 °C on a rocking platform, then spun

828 down for 3 minutes at 300 rcf. The papain solution was replaced with 200 μ L ice-cold

829 EBSS, and the tissue was gently triturated ~10 times with a P1000 pipette to achieve a

830 single-cell suspension. The cells were spun down and resuspended in 200 μ L EBSS for

831 fluorescence activated cell sorting on a FACSAria II machine (BD Biosciences). An

832 aliquot of cells was stained with trypan blue and counted on a haemocytometer. The cell

833 suspension was diluted if necessary with EBSS, aiming for \leq 500,000 cells in a volume

834 of 200 μ L.

835

836 Dissociated cells were labeled with barcoded lipid-modified oligonucleotides (LMOs) as

837 previously published (McGinnis et al., 2019), using a different barcode for each single-

838 litter pooled MGE sample. Excess LMOs and papain were quenched by adding 1 mL of

839 ovomucoid/BSA inhibitor (Worthington). Barcoded cells were spun down for 5 minutes
840 at 500 rcf and resuspended in 300 μ L EBSS with 1% BSA. DAPI (50 ng/mL final
841 concentration) was included to stain dead cells. Just prior to sorting, cells were passed
842 through a 40 μ m filter to remove any remaining clumps.

843
844 GFP-positive cells were isolated by FACS as described above. Cells were sorted into
845 Lo-Bind Eppendorf tubes containing EBSS with 1% BSA. Sorted, barcoded cell samples
846 were then pooled, spun down, and resuspended in a small volume of EBSS with 1%
847 BSA ready for processing on the Chromium 10x system.

848
849 Single-cell cDNA libraries were generated using the Chromium Single Cell 3' GEM,
850 Library & Gel Bead Kit (v3, PN-1000075) according to the manufacturer's instructions.
851 After the first cDNA clean-up step with 0.6x SPRI beads, the supernatant containing the
852 barcode library fraction was saved and processed as described previously (McGinnis et
853 al., 2019). The barcode library (5%) and cDNA library (95%) were pooled for
854 sequencing on an Illumina NovaSeq SP lane.

855

856 **C1 sequencing, alignment, and gene expression quantification**

857 Libraries for the C1 scRNA-seq samples were sequenced on an Illumina HiSeq 4000
858 instrument using a single-end 50-bp protocol. Reads were uniquely aligned to the
859 mouse genome (GRCm38, modified to append a custom chromosome containing the
860 individual sequences of the transgenes CreER^{T2}, IRES, EGFP, and tdTomato) using
861 STAR (v2.7.0e) (Dobin, 2013), and read duplicates were removed using the Picard tools

862 function MarkDuplicates (v2.18.4) (*Picard Toolkit*, 2019). Gene counts were generated
863 using subread featureCounts (v1.6.3) (Liao et al., 2014), to ENSEMBL GRCm38
864 release 95, using a customized gtf annotation file containing annotations for the four
865 transgenes. Gene counts were normalized to gene length and library size using reads
866 per kilobase of transcript, per million mapped reads (RPKM) or to counts per million
867 mapped reads (CPM) for downstream analysis and visualization.

868

869 **10x sequencing, alignment, and gene expression quantification**

870 Libraries for 10x MULTI-seq samples were sequenced on an Illumina NovaSeq SP
871 instrument. The raw 10x data was processed using CellRanger (v3.0.2) (Zheng et al.,
872 2017) using the custom mouse genome described above. Samples were demultiplexed
873 using the MULTI-seq (McGinnis et al., 2019) pipeline ([https://github.com/chris-mcginnis-](https://github.com/chris-mcginnis-ucsf/MULTI-seq)
874 [ucsf/MULTI-seq](https://github.com/chris-mcginnis-ucsf/MULTI-seq)). Briefly, raw FASTQ files were split into cell barcode, UMI, and sample
875 barcode sequences, then reads were parsed to generate a sample barcode UMI count
876 matrix. The cell barcode matrix was put through the MULTI-seq classification workflow
877 to identify single cells from unclassified and doublet/multiplier cells. A second round of
878 semi-supervised classification was performed to reclassify negative cells for potential
879 false negatives. The cell by gene UMI count matrix was loaded into Seurat (v3.2.2)
880 (Butler et al., 2018; Stuart et al., 2019) as a Seurat object, and normalized using the
881 Seurat function *SCTransform* (Hafemeister and Satija, 2019) with default parameters for
882 both full transcriptome and TF-curated analyses.

883

884 **C1 quality control**

885 Raw read quality was assessed using FastQC (v0.11.7) (Andrews, 2010). Aligned
886 library quality was assessed using RSeQC (v2.6.4) (Wang et al., 2012) for 5' or 3' bias,
887 exonic read distribution and GC content distribution. We also assessed quality of
888 individual samples by comparing the following distributions: total uniquely aligned reads,
889 total assigned reads, total expressed genes, percent mitochondrial reads, percent
890 ribosomal genes, and percent pseudogenes. Samples with greater or less than 2
891 standard deviations from the mean in any of the above metrics were discarded. In
892 addition, samples scored as 'two or more cells' during visual inspection were removed
893 from analysis. Pseudogenes, ribosomal genes (ribosomal subunit and rRNAs),
894 mitochondrial genes, and six sex-linked genes (*Xist*, *Eif2s3x*, *Kdm6a*, *Ddx3y*, *Eif2s3y*,
895 *Kdm5d*) (Armoskus et al., 2014) were removed from the data matrix.

896
897 We used the R package Seurat (v3.2.2) (Butler et al., 2018; Stuart et al., 2019) for
898 feature selection, clustering and visualization. We compared two normalization
899 approaches for quality control and downstream analysis. RPKM-normalized data was
900 used to create two Seurat objects, with `minimum.cells` set to 10, and `minimum.genes`
901 set to 2,000. We applied a manual $\log_1 p$ transformation to the RPKM data to generate
902 normalized data in the 'data' slot of the Seurat object. We applied regression for FACS-
903 processing state and total mapped reads on the gene count data using *ScaleData*. To
904 define proliferative state and cell cycle phase, we used the Seurat function
905 *CellCycleScoring* on a published list of cell cycle genes (Kowalczyk et al., 2015) and
906 calculated G1/S and G2/M phase scores for each cell. We then calculated the

907 difference between G1/S and G2/M to define whether a cell was mitotic (M) or post-
908 mitotic (PM).

909

910 We also compared our results to those generated with raw count data normalized using
911 the NormalizeData function with scale.factor set to 1e6 to generate CPM-normalized
912 data. Results were largely similar between RPKM- and CPM-normalized data and only
913 the RPKM-normalized results are reported. We note that short genes were more likely
914 to be considered highly variable using CPM-normalized data (data not shown).

915

916 **10x quality control**

917 We used the MULTI-seq pipeline described above to remove negative or multiplet cells
918 from downstream analysis. After subsetting data to only singlets, we used the full
919 transcriptome data to perform cell clustering with Seurat, which split cells into two
920 populations based on mitochondria RNA (mtRNA) expression: one population with high
921 mtRNA expression (>5% total UMIs) and one with low expression (<5% total UMIs). We
922 removed all cells from the high mtRNA expression population, and repeated cell
923 clustering using the cleaned cells. We identified one outlier cluster likely corresponding
924 to hematopoietic cell lineages based on expression of hemoglobin genes, and removed
925 that cluster, resulting in 4,001 cells for downstream analysis.

926

927 **C1 transcription factor (TF)-based clustering**

928 From the full dataset, we extracted counts for 689 transcription factors with mRNA in
929 situ hybridization data available in the Allen Developing Mouse Brain Atlas (Lein et al.,

930 2007) that were scored for expression in E11.5 and E13.5 basal ganglia and cortex
931 (Table S2). Of the 689 scored transcription factors, 455 were expressed in >10 cells in
932 our dataset. These 455 genes were used for dimensionality reduction using principal
933 components analysis (PCA) and Uniform Manifold Approximation and Projection
934 (UMAP) (McInnes et al., 2018) as visualization tools. Following PCA, we used JackStraw
935 analysis with 100 iterations to define statistically significant (p -value < 0.05) principal
936 components (PCs) driving variation. The first 13 significant PCs were used to define
937 clusters using *FindNeighbors* (using k.param = 5, nn.method = “annoy”, annoy.metric =
938 “euclidean”) and *FindClusters* (using resolution = 1.2, algorithm = 2, group.singletons =
939 F). To generate the UMAP visualization we used Seurat’s *RunUMAP* (reduction = “pca”,
940 n.neighbors = 15, n.epochs = 1000, negative.sample.rate = 10). Using this approach,
941 we defined 12 clusters.

942

943 **10x transcription factor (TF)-based clustering**

944 We used a similar approach as described above for the C1 clustering. Of the 689
945 scored transcription factors, 463 were expressed in greater than 10 cells. These 463
946 genes were used for downstream processing. The first 14 significant PCs were used to
947 define clusters using *FindNeighbors* (using k.param = 15, nn.method = “rann”,
948 annoy.metric = “euclidean”) and *FindClusters* (using resolution = 1.4, algorithm = 2,
949 group.singletons = F). To generate the UMAP visualization we used Seurat’s *RunUMAP*
950 (reduction = “pca”, n.neighbors = 20, n.epochs = 500, negative.sample.rate = 15). Using
951 this approach, we defined 18 clusters.

952

953 **Differential expression analysis**

954 For differential expression (DE) analysis across TF-based clusters in both C1 and 10x
955 datasets, we expanded to all expressed genes and used Seurat's *FindAllMarkers*.
956 Briefly, one cluster of cells was compared to all other cells using a Wilcoxon rank-sum
957 test. We only considered genes that were expressed in at least 25% of cells in either
958 population and had \log_e -fold-change greater than 0.25 between populations. Genes with
959 adjusted p -values < 0.05 were considered statistically significant. We also performed
960 DE analysis between enhancer groups (e.g. MGE-*hs192* vs MGE-*hs799*, or MGE-
961 *hs192*-PM vs MGE-*hs799*-PM) using the same parameters.

962

963 **Diffusion mapping pseudotime analysis**

964 We performed diffusion mapping via the R package *destiny* (Angerer et al., 2016) on the
965 TF-based C1 dataset. Briefly, the log-normalized TF-curated RPKM data was passed to
966 the *destiny* function *dm*, which generates 50 diffusion components and corresponding
967 cell eigenvalues. We assessed differential expression along the diffusion components
968 using a generalized additive model via the *gam* function in R.

969

970 **Random forest classification**

971 We used random forest (Breiman, 2001) via the R package *randomForest* on the TF-
972 based C1 dataset to identify transcription factors important for accurately classifying
973 cells in pairwise comparisons of enhancers. Briefly, we ran *randomForest* independently
974 10 times using the log-normalized TF-curated RPKM C1 data matrix, using 5,000 trees
975 per forest, for each of the pairwise comparisons (MGE-*hs1056*-M vs dMGE-*hs1538*-M;

976 MGE-*hs192*-PM vs MGE-*hs799*-PM; CGE-*hs841*-M vs LGE-*hs841*-M; and CGE-*hs953*-
977 PM vs LGE-*hs599*-PM). We extracted the out-of-box error rates for all forests in addition
978 to the mean decrease in accuracy (MDA) and mean decrease in node impurity (MDNI)
979 scores for all genes, and calculated mean and standard deviation. Genes were ranked
980 by the mean MDA and MDNI scores.

981

982 **Gene ontology analysis**

983 We used the R package topGO (v2.36.0) (Alexa and Rahnenfuhrer, 2020) to perform
984 gene ontology (GO) analysis by TF-based cluster and enhancer group on DE genes in
985 the 10x dataset. Mouse GO data were downloaded from Bioconductor (org.Mm.eg.db)
986 (Carlson, 2019). We restricted analysis to GO Biological Process annotations and
987 required a minimal node size of greater than 20. We used the 'weight01' framework and
988 Fisher test to define significant terms (p -value < 0.05). The background for all
989 enrichment comparisons is all 18,088 expressed genes. For Figure 5, clustering of
990 selected significant GO terms was performed using the R package pheatmap (Kolde,
991 2015) using *hclust* and default parameters.

992

993 **Full transcriptome analysis**

994 We repeated clustering analysis of single cells using the full transcriptome for both C1
995 and 10x scRNA-seq datasets. To define highly variable genes (HVGs), we calculated
996 the mean of all expressed genes in the Seurat object data slot using the Seurat function
997 *FindVariableGenes* using default parameters. The top 3,000 HVGs were used for
998 dimensionality reduction using PCA and UMAP visualization. For C1 data, we used the

999 first 10 PCs to define 11 clusters using *FindNeighbors* (using k.param = 15, nn.method
1000 = "rann", annoy.metric = "euclidean") and *FindClusters* (using resolution = 1, algorithm =
1001 2, group.singletons = F). For 10x data, we used the first 17 PCs to define 17 clusters
1002 using *FindNeighbors* (using k.param = 20, nn.method = "rann", annoy.metric =
1003 "euclidean") and *FindClusters* (using resolution = 1, algorithm = 2, group.singletons =
1004 F). UMAP visualization was generated using *RunUMAP* with the same parameters
1005 described for each dataset above. DE analysis was performed across clusters as
1006 described above.

1007

1008 **Combined analysis of C1 and 10x datasets**

1009 We used canonical correlation analysis (CCA) to combine the C1 and 10x datasets
1010 using both TF-curated and full transcriptome datasets. Briefly, the raw counts for both
1011 datasets were merged together, excluding genes that exhibited expression only in one
1012 dataset, and normalized using *NormalizeData* (normalization.method = "LogNormalize",
1013 scale.factor = 1e6). Integration anchors between both datasets were identified using
1014 *FindIntegrationAnchors* (reduction = "cca", dims = 1:50, normalization.method =
1015 "LogNormalize", anchor.features = 3000). Datasets were integrated using 50 CCA
1016 components from *FindIntegrationAnchors* with *IntegrateData* (dims = 1:50), and center-
1017 scaled data generated using *ScaleData*. The integrated dataset was used for principal
1018 components analysis and the first 15 PCs were used to define 17 clusters using
1019 *FindNeighbors* (using k.param = 5, nn.method = "rann", annoy.metric = "euclidean") and
1020 *FindClusters* (using resolution = 1, algorithm = 2, group.singletons = F). UMAP

1021 visualization was generated using *RunUMAP* (reduction = “pca”, n.neighbors = 20,
1022 n.epochs = 1000, negative.sample.rate = 10).

1023

1024 **ABA ISH transcription factor scoring**

1025 Expression levels of all transcription factors in the Allen Developing Mouse Brain Atlas
1026 (Lein et al., 2007) were estimated in subdomains of the subpallium for two ages: E11.5
1027 and E13.5. The subpallium was divided into 4 anatomical domains (LGE, MGE,
1028 Septum, and POA). The LGE and MGE were further subdivided into laminar
1029 subdomains: VZ/SVZ and MZ for E11.5; VZ, SVZ1, SVZ2, and MZ for E13.5.

1030 Expression was annotated from sagittal sections in each subdomain as an Intensity
1031 value and a Density value on a 0-5 scale. The intensity value was derived from the
1032 color-coded intensity viewing option called “expression mask” on the ABA. The density
1033 value was assigned by binning the frequency of individual signals across subdomains
1034 onto the 0-5 scale.

1035

1036 **Histology**

1037 *Section preparation.*

1038 Pregnant dams were sacrificed by CO₂ inhalation, confirmed by cervical dislocation.
1039 E11.5 embryos were removed and placed into ice-cold 1x PBS. The heads were cut off
1040 and drop-fixed in 4% paraformaldehyde in PBS overnight at 4 °C. The fixed heads were
1041 then cryoprotected in 20% sucrose in PBS overnight at 4 °C, embedded in OCT
1042 compound (TissueTek) and frozen on dry ice. Cryostat sections 15 µm thick were cut
1043 directly onto SuperFrost slides and allowed to dry.

1044

1045 *Fluorescent immunohistochemistry.*

1046 Sections were rinsed in PBS, blocked for 1 hour at room temperature in PBST (PBS +
1047 0.25% Triton X-100) with 10% FBS, and incubated with primary antibody diluted in
1048 PBST + 10% FBS overnight at 4 °C. Primary antibodies used were mouse anti-Tle4
1049 (1:100, Santa Cruz Biotechnology, #sc-365406, RRID: AB_10841582), rat anti-GFP
1050 (1:1000, Nacalai Tesque, #04404-84, RRID: AB_10013361) and rabbit anti-GFP
1051 (1:5000, Abcam, #ab6556, RRID: AB_305564). The following day, sections were
1052 washed 2 x 15 min in PBST and 2 x 15 min in PBS, incubated for 2 hours at room
1053 temperature with Alexa fluor-conjugated secondary antibodies (1:750, Invitrogen).
1054 Finally, sections were washed 2 x 15 min in PBST and 2 x 15 min in PBS and
1055 coverslipped with Fluorescence Mounting Medium (DAKO #S3023).

1056

1057 *Fluorescence in situ hybridization (FISH).*

1058 The antisense RNA probes used in this study have been described previously (Long et
1059 al., 2009). In situ hybridization was performed on 15 µm cryostat sections as described
1060 previously (Lindtner et al., 2019) up until the antibody blocking step, with the addition of
1061 a peroxidase quenching step for 20 minutes in 3% H₂O₂ in PBS after the SSC washes.
1062 After blocking, slides were incubated with anti-Digoxigenin-POD Fab fragments (Roche
1063 #11207733910) diluted 1:500 in NTT blocking buffer for 1 hour at room temperature.
1064 Slides were then washed for 3 x 5 minutes in NTT and developed with Cy5-Tyramide
1065 signal amplification reagent (TSA Plus Kit, Akoya Biosciences #NEL745001KT)
1066 according to the manufacturer's instructions. Finally, sections were washed 3 x 15

1067 minutes in PBS, incubated for 5 minutes with nuclear counterstain Hoechst 33342
1068 (1:1000 in PBS, ThermoFisher #H3570), rinsed 3 x 5 minutes in PBS, and coverslipped
1069 with Fluorescence Mounting Medium (DAKO #S3023).

1070

1071 *Imaging.*

1072 Low-magnification epifluorescent images were taken using a Coolsnap camera
1073 (Photometrics) mounted on a Nikon Eclipse 80i microscope using NIS Elements
1074 acquisition software (Nikon) and a 4x or 10x objective. Confocal images were taken with
1075 20x air and 40x oil objectives on an Andor Borealis CSU-W1 spinning disk confocal
1076 mounted on a Nikon Ti Microscope and captured with an Andor Zyla sCMOS camera
1077 and Micro-Manager software (Open Imaging). The raw images were pre-processed with
1078 ImageJ software (v2.0.0) to adjust brightness/contrast and convert to 8-bit RGB.
1079 Confocal images were stitched laterally to create composites using the Grid/Collection
1080 stitching ImageJ plugin with linear blending (Preibisch et al., 2009).

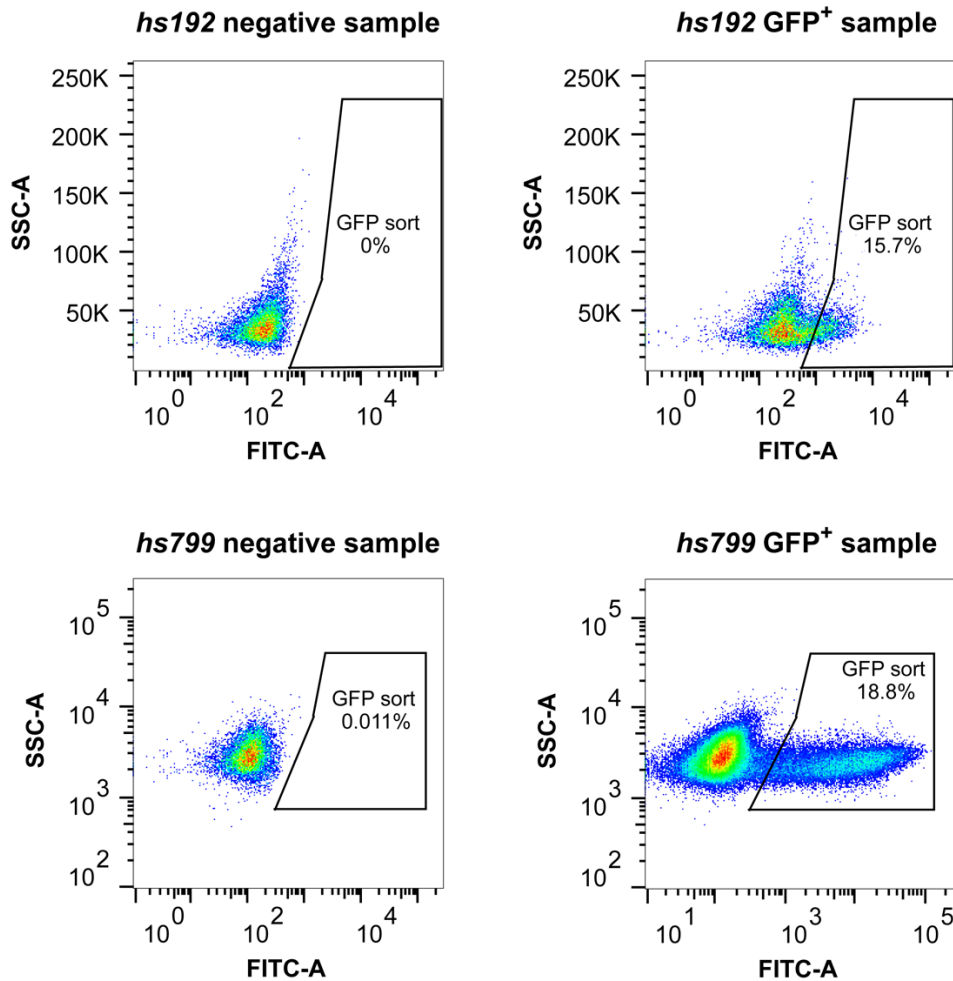
1081

1082 *Cell counts.*

1083 Cell counting was performed on single confocal image planes in ImageJ using the Cell
1084 Counter plugin. Counts were summed from at least 3 rostrocaudal sections for each
1085 brain. Tle4-positive cells were counted first with the GFP channel hidden, excluding
1086 cells in the VZ (designated by nuclear staining), then scored as positive or negative for
1087 overlap with GFP staining.

1088

1089 **Supplementary Figures**
1090

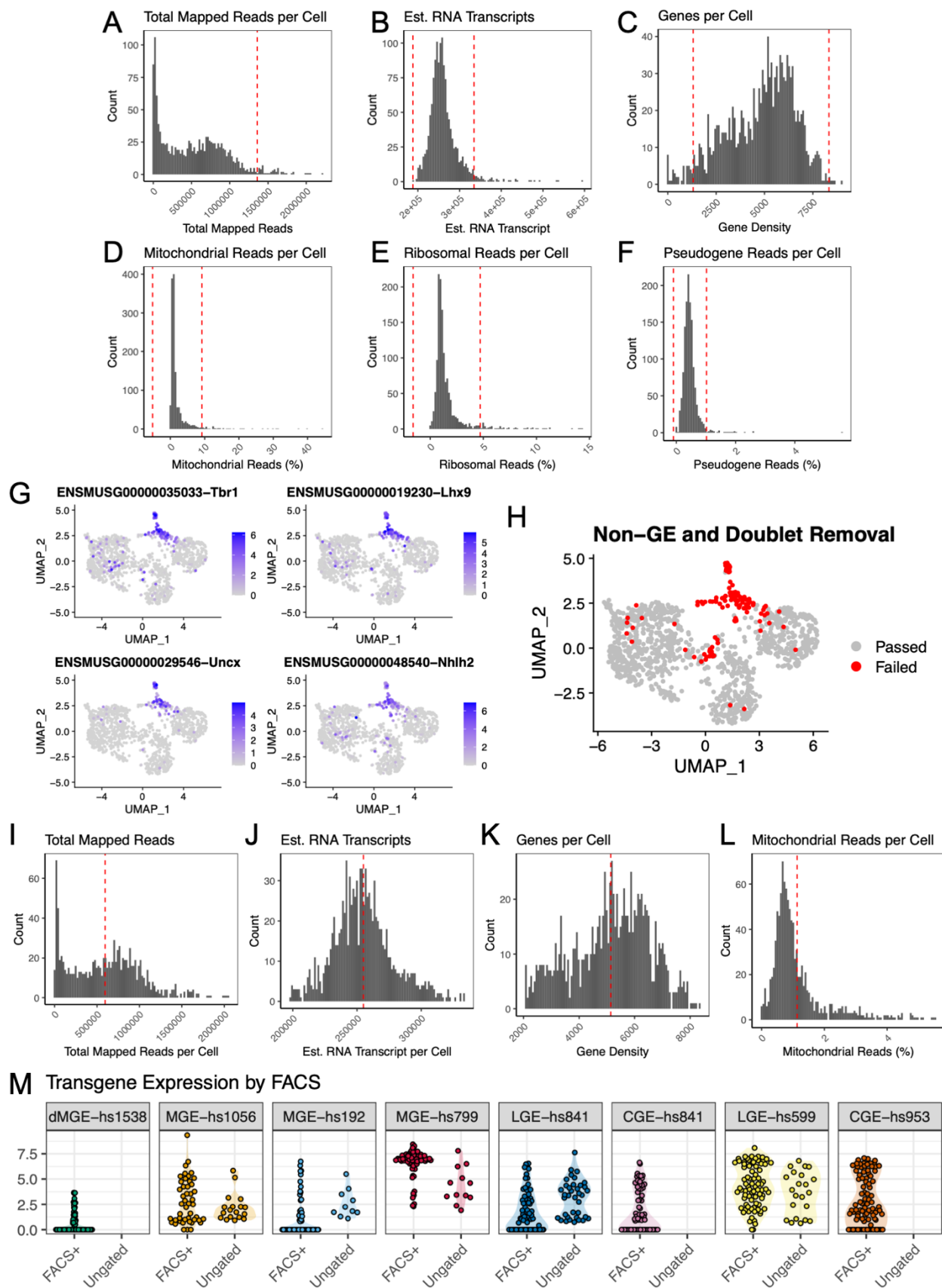


1091

1092

1093 **Supplementary Figure 1: FACS gating schematics.**

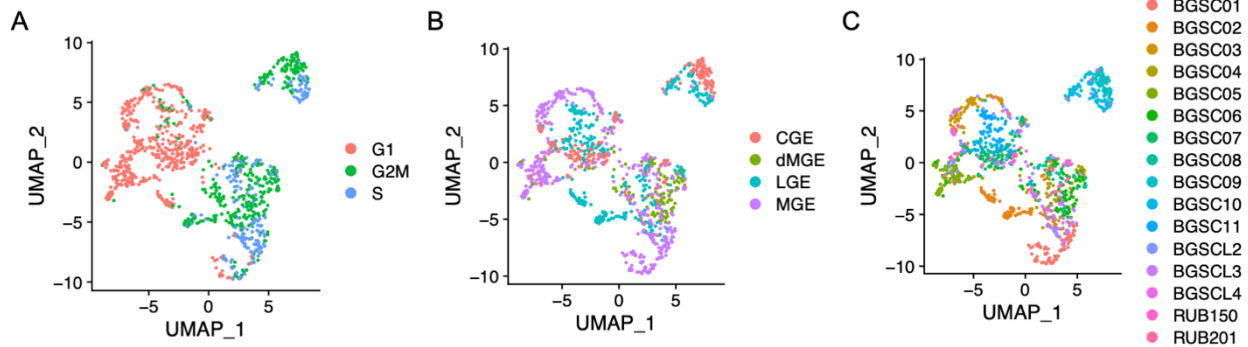
1094 Density plots showing side-scatter (SSC) versus GFP fluorescence intensity (FITC) for
1095 negative and GFP-positive samples from *hs192* and *hs799* MGE. GFP sort area shows
1096 cells collected for scRNA-seq and the percentage of live cells captured. Negative
1097 samples were used to set the gating. *hs799*⁺ cells show brighter GFP fluorescence than
1098 *hs192*⁺ cells.



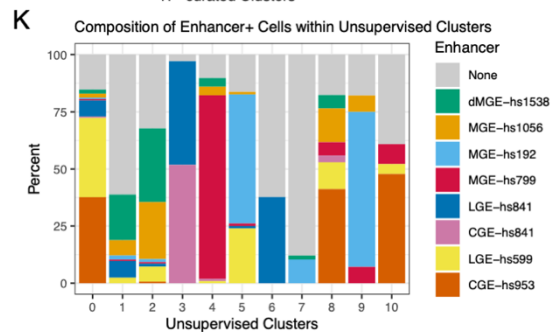
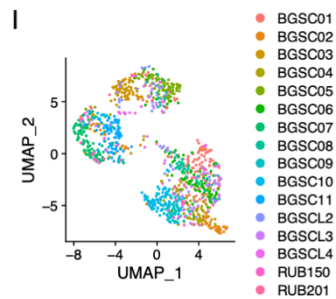
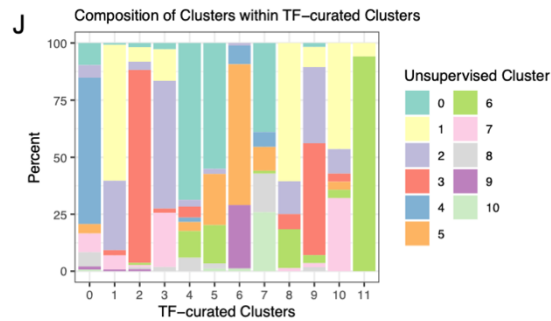
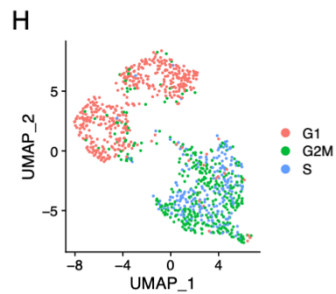
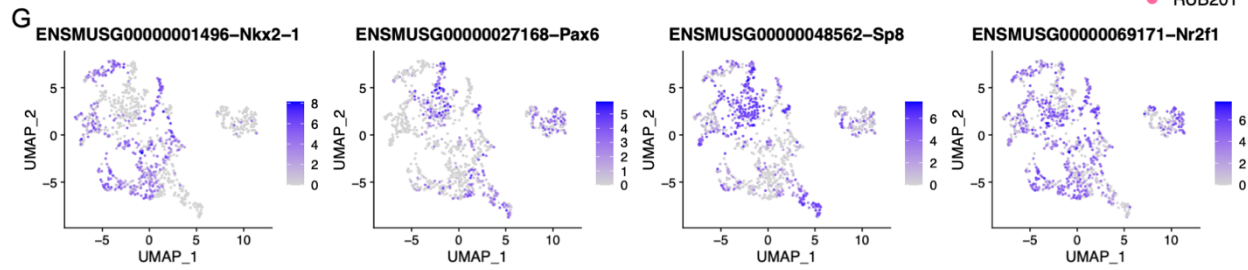
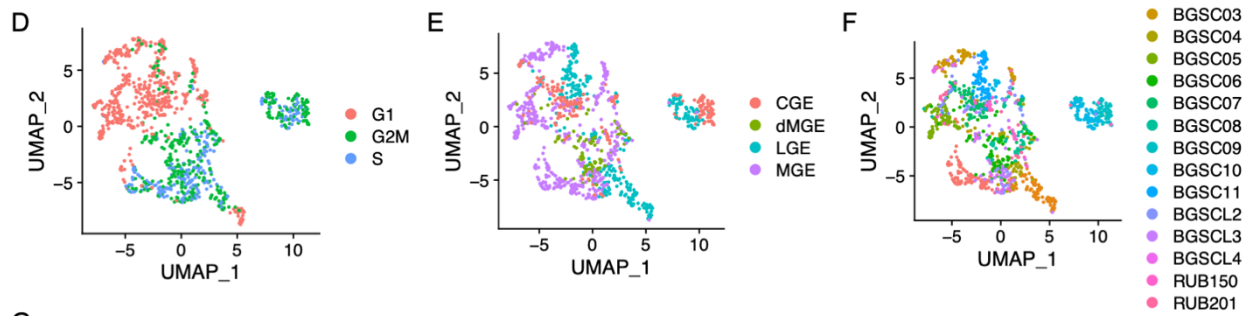
1100 **Supplemental Figure 2: C1 scRNA-seq quality control.**

1101 **(A-F)** Histogram of total uniquely mapped reads **(A)**, estimated RNA transcript **(B)**,
1102 number of expressed genes **(C)**, percent mitochondrial reads **(D)**, percent ribosomal
1103 reads **(E)**, and percent pseudogenes **(F)** per cell, post-duplication removal for all
1104 sequenced samples. Cells above or below the red lines were removed from
1105 downstream analysis. Red lines represent mean \pm 2 s.d. **(G)** UMAP of transcription-
1106 factor-curated clusters after removal of cells flagged in A-F, colored by normalized
1107 expression of four genes used for flagging cells as non-ganglionic in origin (*Tbr1*, *Lhx9*,
1108 *Uncx*, and *Nhlh2*). **(H)** UMAP colored by quality control flag for contaminating cells and
1109 suspected doublets (passed: used for downstream analysis; failed: removed from
1110 downstream analysis). **(I-L)** Histograms of total mapped reads **(I)**, estimated RNA
1111 transcripts **(J)**, expressed genes per cell **(K)**, and percent mitochondrial reads per cell
1112 **(L)**, for all cells that passed final quality control. Red line represents mean. **(M)**
1113 Normalized transgene expression for each of the seven enhancers profiled, separated
1114 by FACS⁺ gating or no FACS⁺ gating (if performed).

HVG (n = 3000) clustering by cell cycle phase, dissection, and sequencing lane without cell cycle regression



HVG (n = 3000) clustering by cell cycle phase and dissection after cell cycle regression

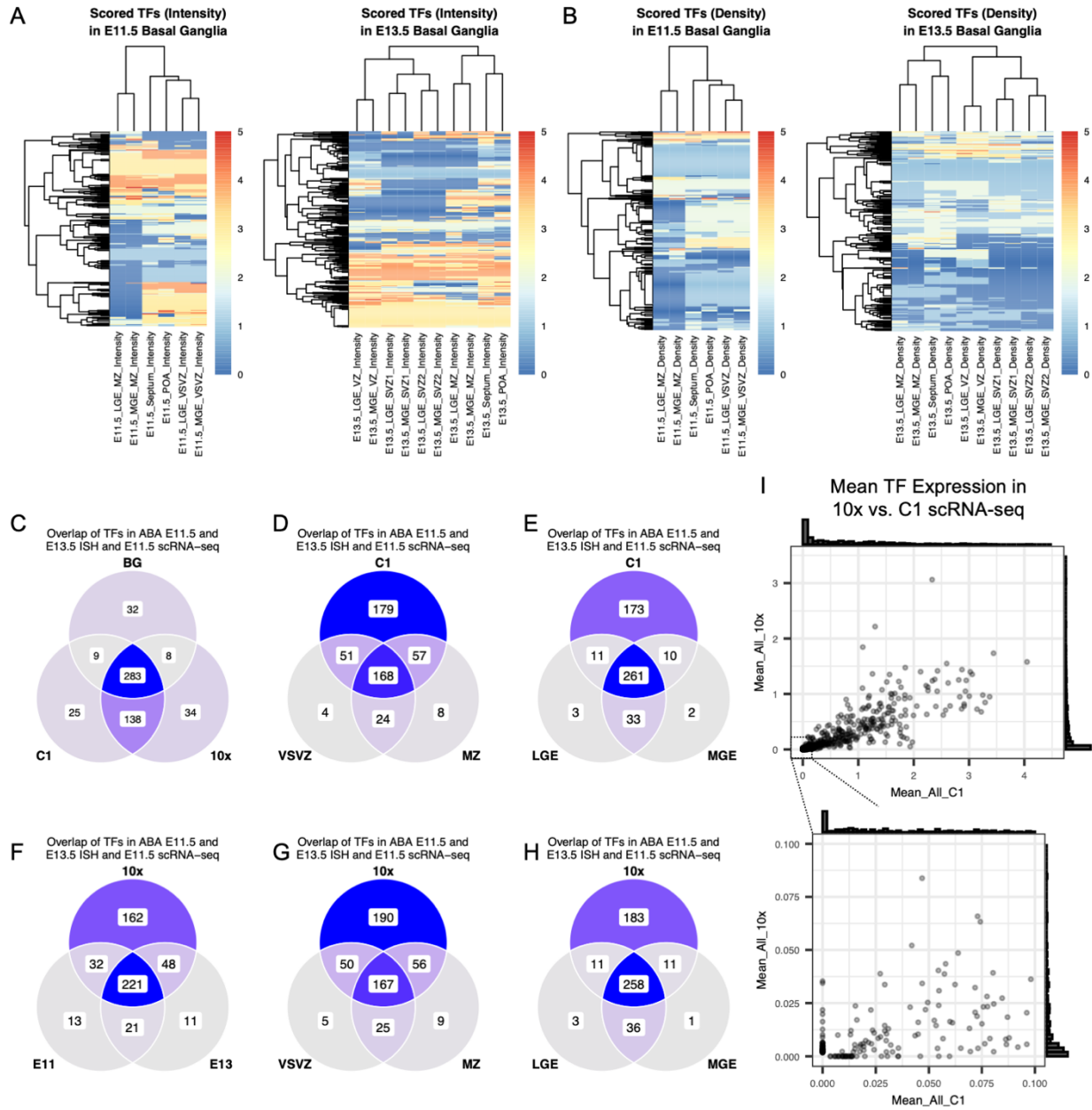


1116

1117 **Supplemental Figure 3: Comparison between full transcriptome and TF-curated**
1118 **analyses for C1 scRNA-seq.**

1119 **(A-C)** UMAP representations using full transcriptome (“unsupervised”) clustering of the
1120 top 3,000 highly variable genes (HVGs) with no cell cycle phase regression, colored by
1121 cell cycle phase **(A)**, region of dissection **(B)**, and sequencing lane **(C)**. **(D-F)** UMAP
1122 representations using full transcriptome of the top 3,000 highly variable genes (HVGs)
1123 after cell cycle phase regression, colored by cell cycle phase **(D)**, region of dissection
1124 **(E)**, and sequencing lane **(F)**. **(G)** UMAP colored by normalized expression of four
1125 region-defining transcription factors (*Nkx2-1*, *Pax6*, *Sp8*, and *Nr2f1*). **(H)** TF-curated
1126 UMAP colored by cell cycle phase. **(I)** TF-curated UMAP colored by sequencing lane.
1127 **(J)** Bar plot of TF-curated clusters by percent representation from unsupervised (full
1128 transcriptome) clusters. Some unsupervised clusters (e.g. cl-10, light green) remain
1129 consistent between clustering methods, while others (e.g. cl-1, light yellow) are split
1130 across multiple TF-curated clusters. **(K)** Bar plot of unsupervised clusters by enhancer
1131 representation. Some enhancers (e.g. MGE-*hs799*, red) are relatively consistent across
1132 clustering methods, while others (e.g. MGE-*hs192*, light blue) split across clusters.

1133



1134

1135

1136 **Supplemental Figure 4: Allen Developing Mouse Brain Atlas and scRNA-seq**

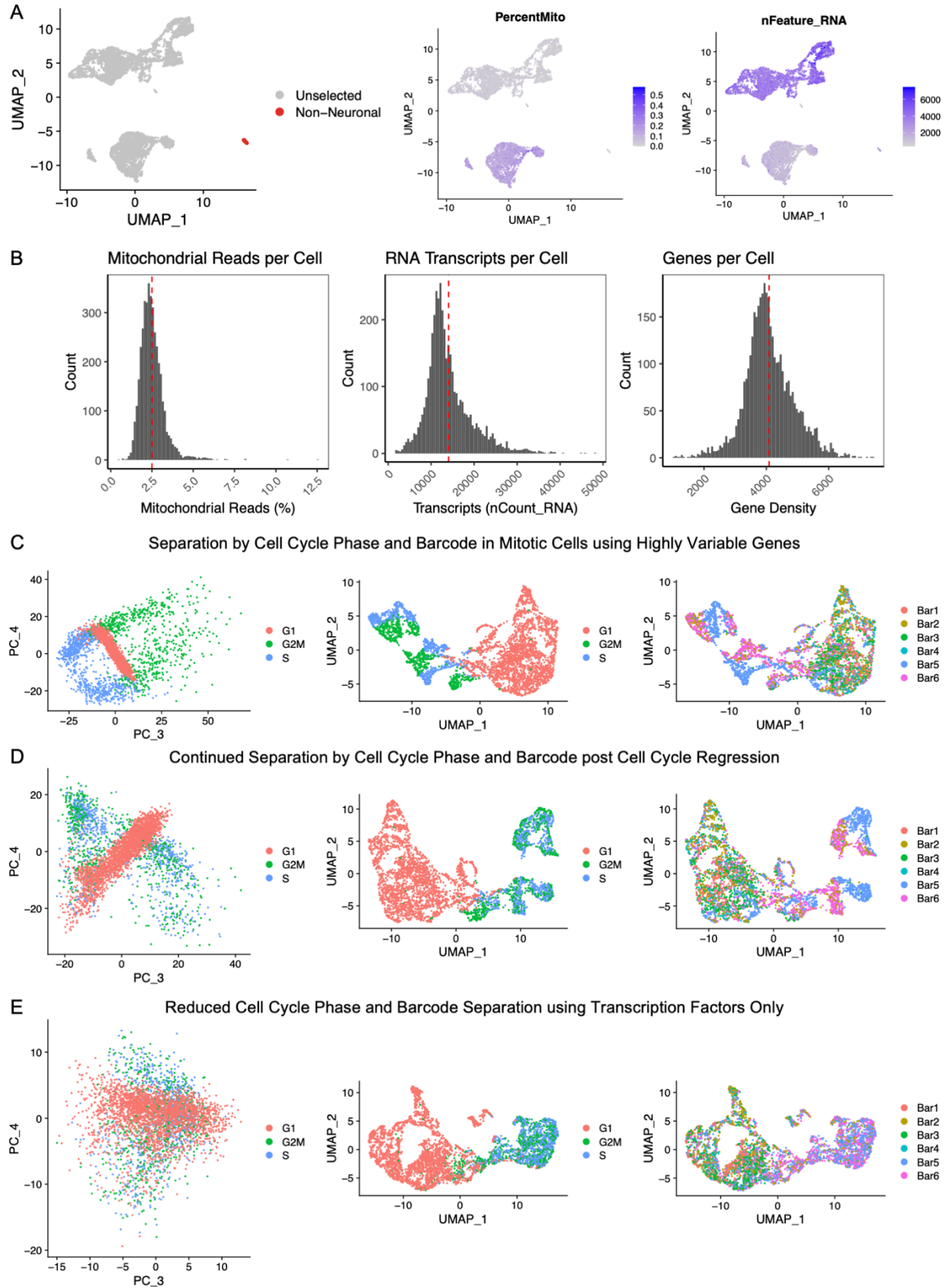
1137 **overlaps.**

1138 **(A)** Heatmap for E11.5 (*left*) and E13.5 (*right*) scored transcription factor (TF)

1139 expression by intensity in Allen Developing Mouse Brain Atlas (ABA) RNA in situ

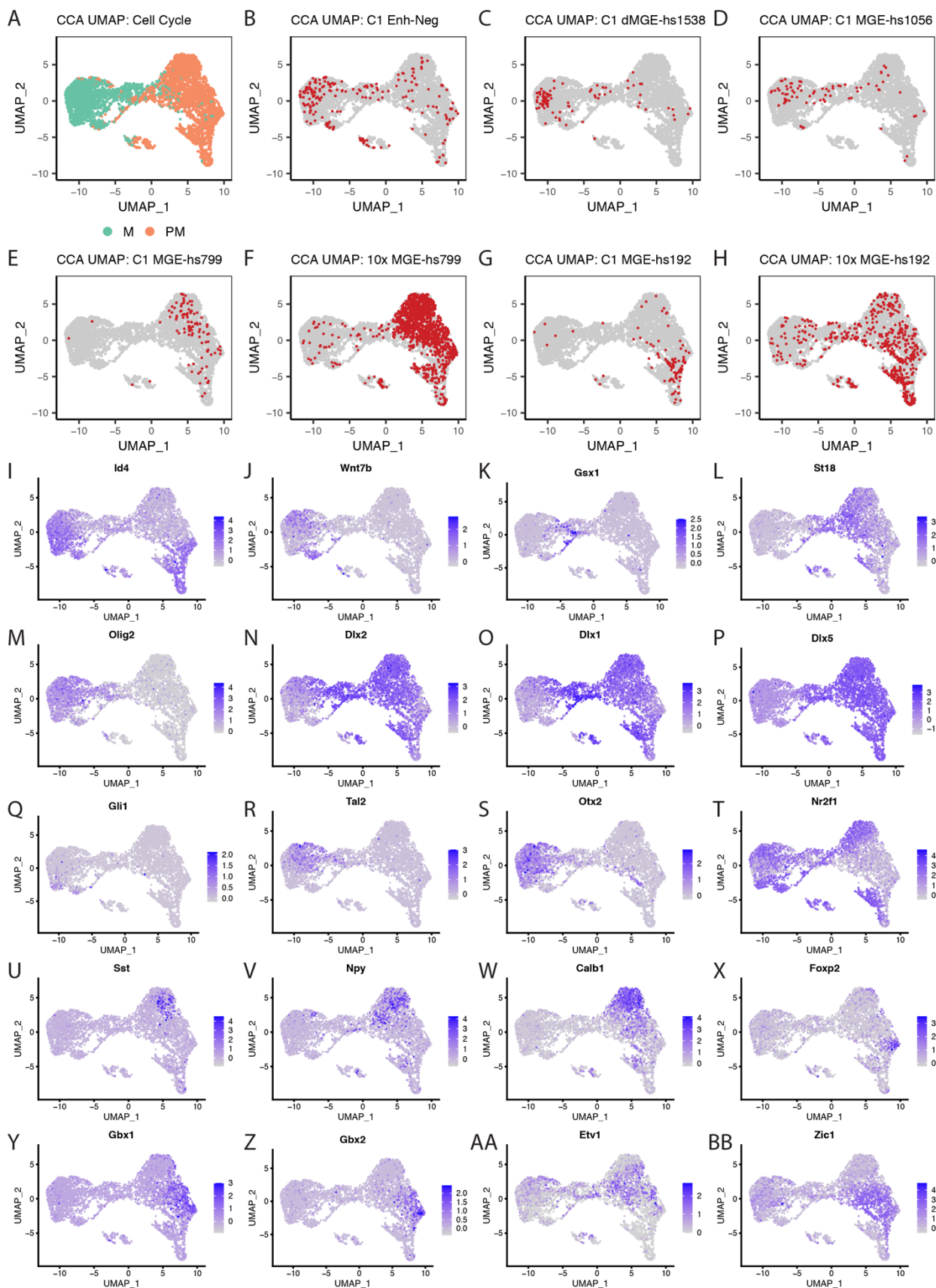
1140 hybridization (ISH) for 689 TFs. Rows: transcription factors; columns: areas and time

1141 points scored. MGE: medial ganglionic eminence; LGE: lateral ganglionic eminence;
1142 POA: preoptic area; VSVZ: ventricular/subventricular zone; MZ: mantle zone. **(B)**
1143 Heatmap of scored expression as in (A), by density. **(C)** Venn diagram of overlap of TFs
1144 with non-zero intensity score in E11.5 and E13.5 basal ganglia (MGE and LGE
1145 combined) from the ABA dataset (“BG”) to detected TFs in C1 and 10x scRNA-seq
1146 datasets. **(D-E)** Overlap of TFs expressed in C1 scRNA-seq, separated by non-zero
1147 VSVZ vs MZ intensity scores **(D)** or LGE vs MGE scores **(E)** in E11.5 and E13.5 ABA
1148 ISH. **(F)** Overlap of TFs expressed in 10x scRNA-seq, separated by non-zero intensity
1149 scores in E11.5 vs E13.5 ABA ISH. **(G-H)** Overlap of TFs expressed in 10x scRNA-seq,
1150 separated by non-zero VSVZ vs MZ intensity scores **(G)** or LGE vs MGE scores **(H)** in
1151 E11.5 and E13.5 ABA ISH. **(I)** (*Top*) Plot comparing mean normalized expression of
1152 transcription factors between 10x and C1 scRNA-seq. Cell distribution along x- and y-
1153 axes are represented by histograms. (*Bottom*) Enlargement of the bottom-left corner of
1154 the top panel, showing distribution of low-representation TFs and dataset-specific
1155 expression.



1157 **Supplemental Figure 5: 10x scRNA-seq quality control.**

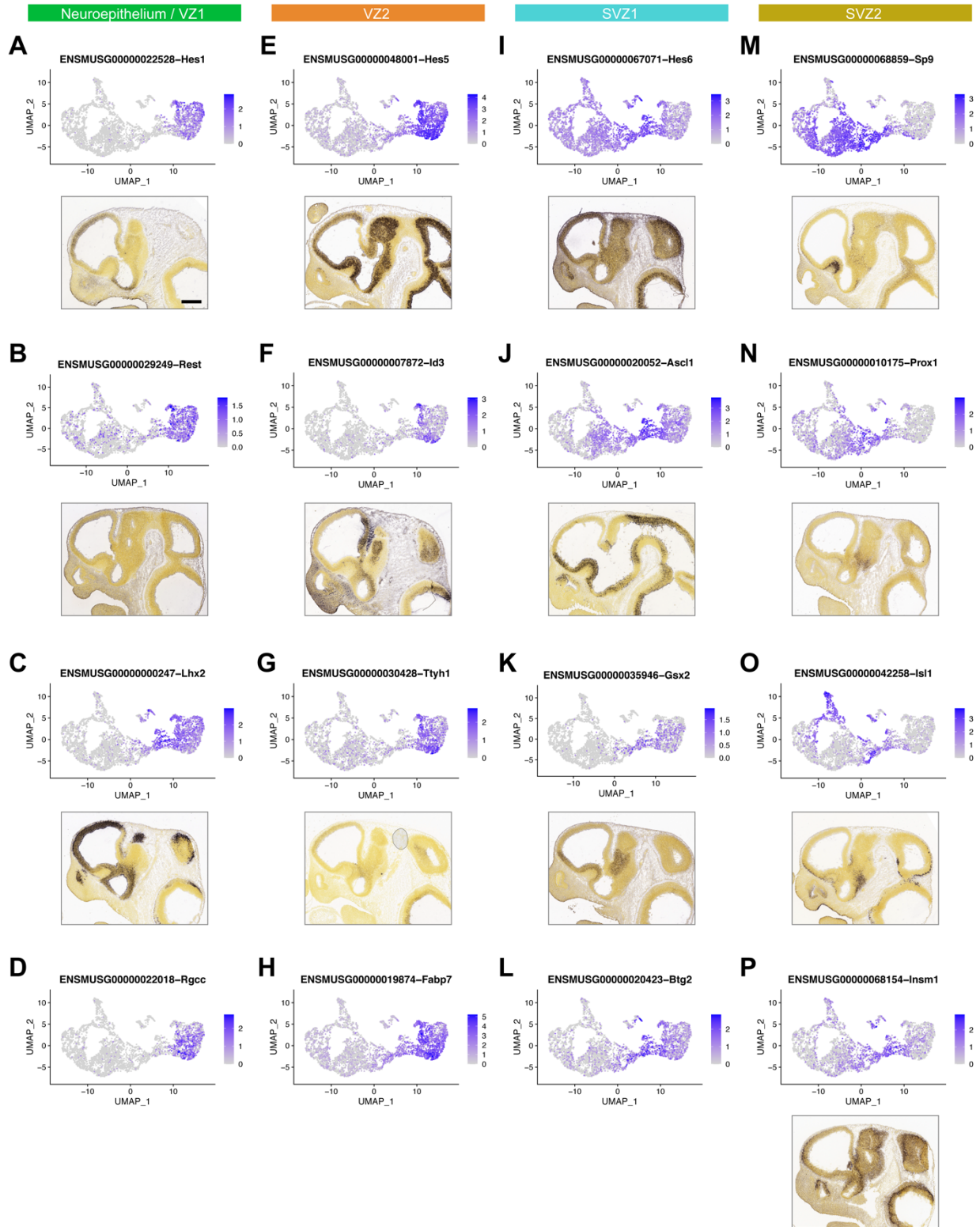
1158 **(A)** UMAP representation of single cells after sample demultiplexing and removal of
1159 multiplets using the MULTI-seq pipeline, colored by cells flagged for likely non-neuronal
1160 origin (*left*), percent mitochondrial reads, (*middle*), and number of expressed genes per
1161 cell (*right*). **(B)** Distribution of percent mitochondrial reads (*left*), estimated RNA
1162 transcripts (*middle*), and number of expressed genes per cell (*right*) with means (red
1163 line) after removal of all cells flagged by quality control metrics (effectively cells
1164 $UMAP_2 < 0$ in A). **(C)** Principal components (PCs) 3 and 4 separate mitotic cells by cell
1165 cycle phase in full transcriptome (unsupervised) clustering using the top 3,000 highly
1166 variable genes (HVGs) (*left*). In UMAP representation of unsupervised clustering, cells
1167 separate by cell cycle phase (*middle*) and MULTI-seq barcode (*right*) in mitotic cells. **(D)**
1168 After cell cycle regression, cell cycle phase separation is negated (*left* and *middle*) but
1169 cells still separate by barcode in mitotic cells (*right*). **(E)** Using transcription factor-based
1170 clustering, both cell cycle phase separation (*left* and *middle*) and barcode separation
1171 (*right*) are negated.



1173 **Supplemental Figure 6: Canonical correlation analysis between C1 and 10x MGE**

1174 **scRNA-seq datasets.**

1175 **(A)** TF-curated UMAP of combined C1 and 10x scRNA-seq using canonical correlation
1176 analysis, colored by mitotic state (green: mitotic; orange: postmitotic) **(B-H)** UMAP plots
1177 colored by C1 or 10x enhancer group. Red: selected group; grey: all other cells. **(I-BB)**
1178 UMAP plots of normalized gene expression for genes shown in Figure 5 (I-T) and
1179 Figure 6 (U-BB).



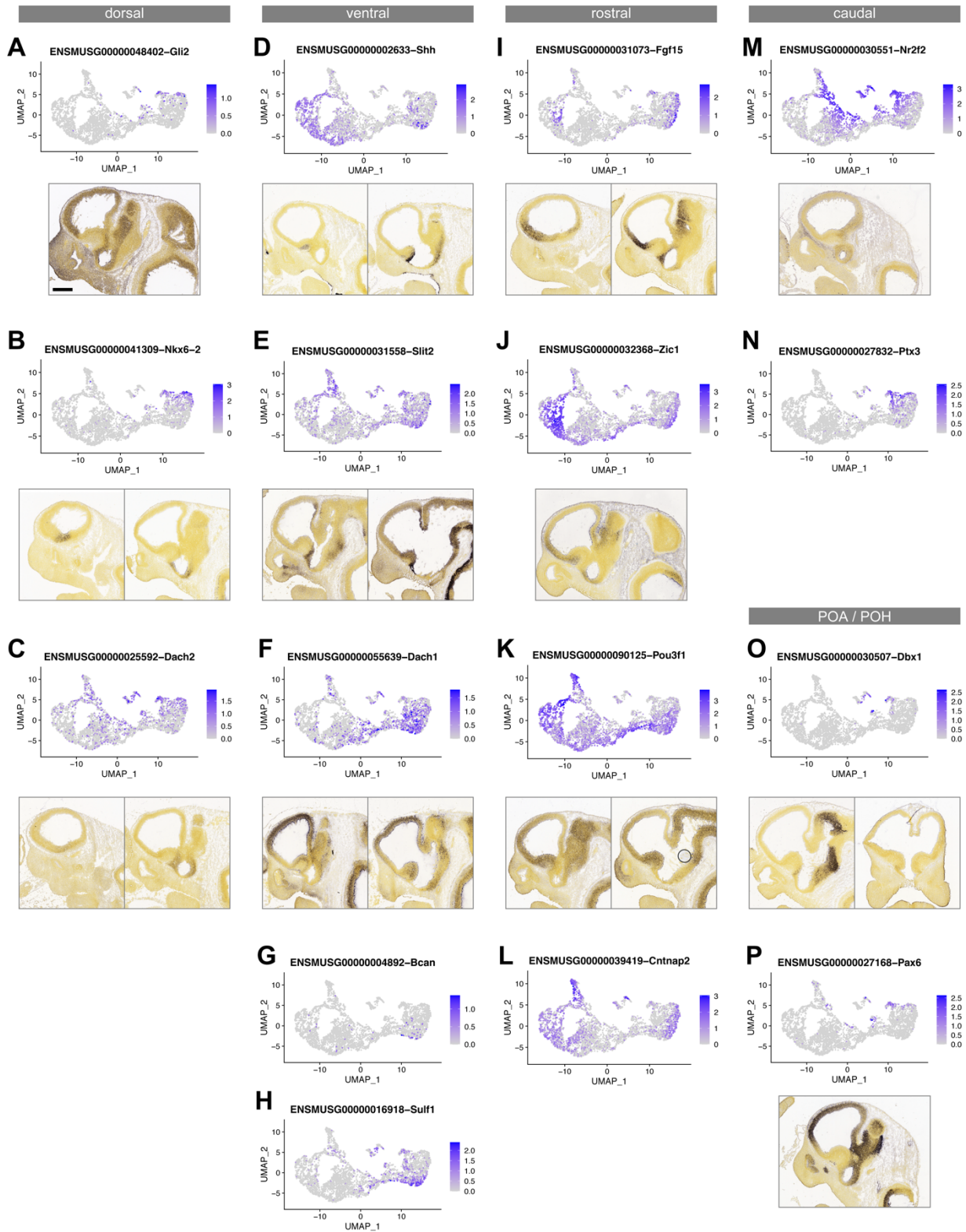
1180

1181

1182

1183 **Supplementary Figure 7: Mitotic genes marking VZ/SVZ transitions.**

1184 **(A-F)** Gene expression UMAPs and representative ISH on E11.5 sagittal sections from
1185 the ABA showing expression of genes that correlate with developmental progression
1186 from early VZ1 (neuroepithelium) to late SVZ (SVZ2). Scale bar: 500 μ m.

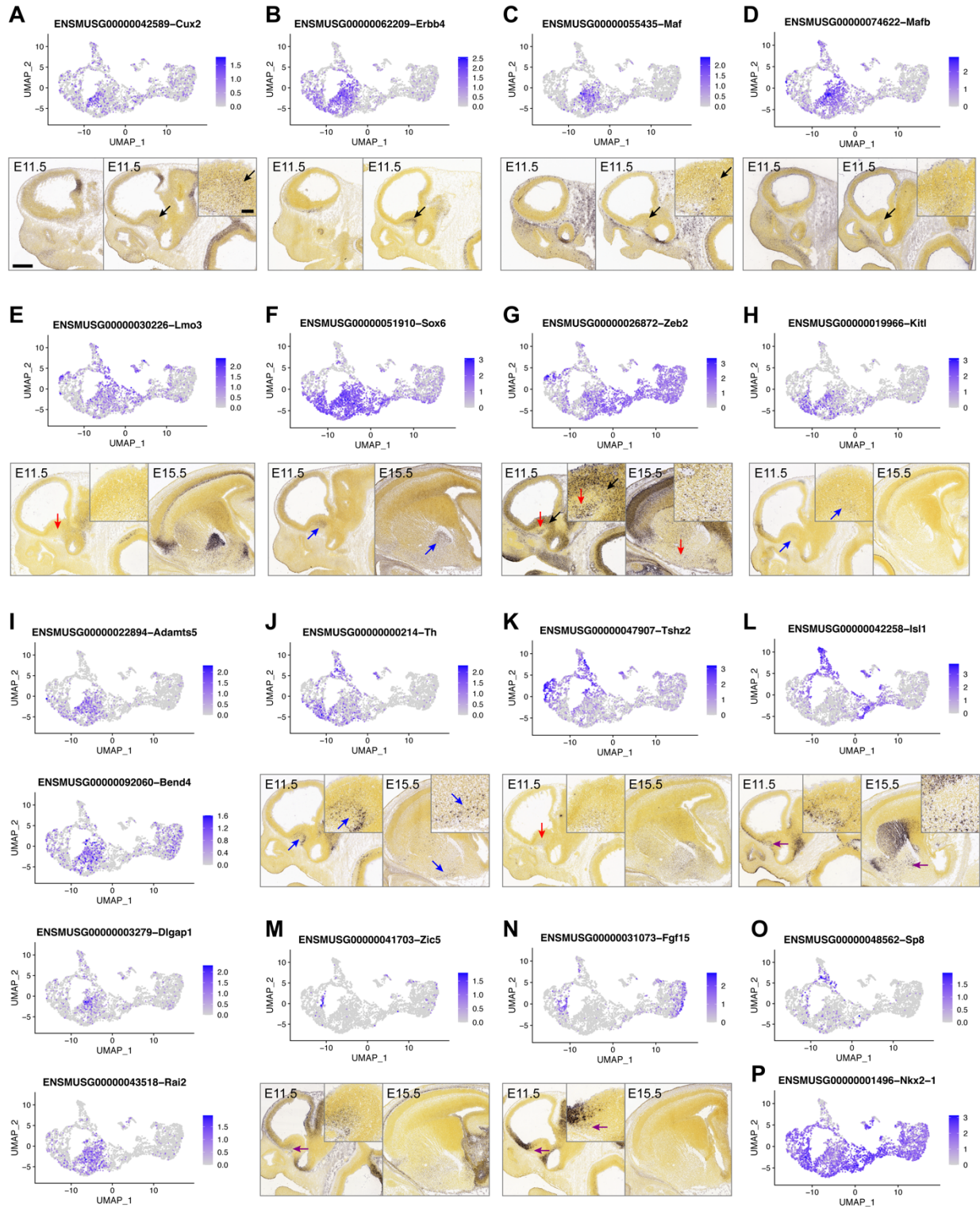


1187

1188

1189 **Supplementary Figure 8: Mitotic genes with dorsoventral or rostrocaudal bias.**

1190 **(A-H)** Gene expression UMAPs and representative ISH on E11.5 sagittal sections from
1191 the ABA showing genes with dorsal (*Gli2*, *Nkx6-2*, *Dach2*) or ventral (*Shh*, *Slit2*, *Dach1*,
1192 *Bcan*, *Sulf1*) bias in mitotic cells. *Dach2*, *Dach1*, *Bcan* and *Sulf1* regional expression in
1193 the MGE has not been reported previously. **(I-N)** Gene expression UMAPs and
1194 representative ISH on E11.5 sagittal sections from the ABA showing genes with
1195 rostrocaudal bias in mitotic cells (*Nr2f2*, *Ptx3*, *Fgf15*, *Cntnap2*, *Zic1*, *Pou3f1*). **(O,P)**
1196 UMAP plots and ISH images of genes marking POA2 (*Dbx1*) or POH (*Pax6*) VZ cells.
1197 These cells are contiguous with the caudal MGE anatomically and in the UMAP. Scale
1198 bar: 500 μ m.



1199

1200

1201

1202 **Supplementary Figure 9: Genes marking classes of postmitotic neurons.**
1203 **(A-D)** Gene expression UMAPs and representative ISH on E11.5 sagittal sections from
1204 the ABA showing expression of markers for early CINs (*Cux2*, *ErbB4*, *Maf*, *Mafb*). **(E-H)**
1205 Gene expression UMAPs and representative ISH for genes marking CINs and classes
1206 of projection neurons (*Lmo3*, *Sox6*, *Zeb2*, *Kitl*). **(I)** Gene expression UMAPs of proposed
1207 novel early CIN markers (*Adamts5*, *Bend4*, *Dlgap1*, *Rai2*). **(J-N)** Gene expression
1208 UMAPs and representative ISH for genes marking classes of MGE-derived projection
1209 neurons (*Th*, *Tshz2*) or cholinergic neurons (*Isl1*, *Zic5*, *Fgf15*). **(O,P)** UMAPs of *Sp8* and
1210 *Nkx2-1* showing the separation of cl-7 into an *Sp8*-positive non-MGE zone and an
1211 *Nkx2-1*-positive MGE-derived zone. Arrows indicate regions of higher magnification
1212 insets and cells of interest. Arrow colors: black, CINs; red, VP; blue, GP; purple; Ch.
1213 Scale bars: low magnification, 500 μm ; high magnification insets, 100 μm .

Subpallium			Flames et al. (2007)	Derivatives			Migr. inter-neur.
Parts	Domains	Other		superficial	middle	deep	
St	seSt		pSe1-3	?	?	?	
	pseSt			OTacb	AcbSh	AcbCo	
	cSt <div style="display: inline-block; vertical-align: middle; margin-left: 10px;"> </div>	radial parts		OTst	Put VSt LSt	Cau	
		dorso-ventral parts	Std Stv StPal	pLGE1 pLGE2-3 pLGE4	Pax6 cells Matrix and striosomes Striopallidal transition		
	aSt			ICa	CeC	ASt	
Pal	sePal		pSe4	?	?	?	
	psePal		pMGE0-4			BSTpal	
	cPal <div style="display: inline-block; vertical-align: middle; margin-left: 10px;"> </div>	rostral	pMGE0-4		GPe VPal	BSTpal	
		caudal	pMGE0-4	OTpal	OTpal	VPal	BSTpal
	aPal			MeA	CeM		
Dg	seDg		pSe5	MSe (migr ChAT cells)			
	pseDg		pMGE5	DBV		BSTdg	
	cDg	rostral	pMGE5	OTdg	VDg	GPi	
		caudal	pMGE5	DBH	SI-Bas-MCPO	BSTdg	x (E11.5)
aDg			AA	CeL	BSTA		
Poa	sePoa		pSe6	SeCPoa			
	psPoa		pPOA1	MnPO			
	cPoa <div style="display: inline-block; vertical-align: middle; margin-left: 10px;"> </div>	Poa1	pPOA1	LPO	LPO	LPO	
		Poa2	pPOA2	MPO	MPO	MPO	
aPoa	PoH	pPOH	?	?	?		

1214

1215

1216 **Supplementary Table 6: Proposed origins of subpallial neurons.**

1217 Proposed origins of subpallial neurons, based on a body of anatomical, developmental

1218 and genoarchitectural findings (Puelles et al., 2016, 2013; Silberberg et al., 2016). Here

1219 we compared the nomenclature from this paper with that from (Flames et al., 2007). The

1220 left 3 columns (Subpallium) list the progenitor domains and subdomains: Column 1)
1221 Parts (major subdivisions): Striatum (St), Pallidum (Pal), Diagonal (Dg) and Preoptic
1222 Area (POA). Column 2) Domains (shared pattern across all the parts of septal,
1223 paraseptal, central and amygdalar regions, distinguished along the septoamygdalar
1224 axis): For St [septal St (seSt), paraseptal St (pseSt), central St (cSt), and amygdalar St
1225 (aSt)], for Pal [septal Pal (sePal), paraseptal Pal (psePal), central Pal (cPal), amygdalar
1226 Pal (aPal)], for Dg [septal Dg (seDg), paraseptal Dg (pseDg), central Dg (cDg), and
1227 amygdalar Dg (aDg)], and for Poa [septal Poa (sePoa), paraseptal Poa (psePoa),
1228 central Poa (cPoa), and amygdalar Poa (aPoa)]. Column 3) Other: provides
1229 morphological information on alternative subdivisions distinguished either along the
1230 radial dimension or the dorsoventral dimension. The central column lists the
1231 corresponding progenitor domains proposed in (Flames et al., 2007). Right columns
1232 (Derivatives) list the known neuronal derivatives of the subpallial progenitor domains,
1233 organized into radial (laminar) positions: superficial (closest to the pia), middle and deep
1234 (closest to the ventricle). The column on the far right (migrating interneurons) lists data
1235 from this publication proposing that the caudal Dg is the source for interneurons at
1236 E11.5. Other publications provide evidence that other subpallial progenitors also
1237 generate interneurons (for the pallium, striatum and olfactory bulb) at later ages.
1238
1239 Other abbreviations, in the order that they are listed in the Table: OTacb (accumbens
1240 part of the olfactory tubercle), AcbSh (shell of the accumbens), AcbCo (core of the
1241 accumbens), OTst (central striatal part of the olfactory tubercle), Put and Cau (Putamen
1242 and Caudate, derivatives of the dorsal striatum, DSt), Vst, LSt (Ventral Striatum and

1243 Lateral Striatum, derivatives of the Ventral Striatum), Ica (intercalated nuclei of the
1244 amygdala), CeC (capsular part of the central amygdala), ASt (amygdalo-striatal
1245 transitional area), BSTpal (pallidal part of bed nucleus stria terminalis), GPe (external
1246 globus pallidus), VPal (ventral pallidum), OTpal (pallidal part of olfactory tubercle), MeA
1247 (medial amygdala), CeM (medial part of the central amygdala), MSe (medial septum,
1248 with cholinergic ChaAT neurons that may have migrated in from another region), DBV
1249 (diagonal band, vertical limb), BSTdg (diagonal part of bed nucleus stria terminalis),
1250 OTdg (diagonal part of olfactory tubercle), VDg (ventral diagonal area, GPi (internal
1251 globus pallidus), DBH (diagonal band, horizontal limb), SI-Bas-MCPO (substantia
1252 innominata, nucleus basalis, magnocellular preoptic complex), AA (anterior amygdala),
1253 CeL (lateral part of the central amygdala), BSTA (amygdalar part of BST), SeCPOA
1254 (septocommissural POA), MnPO (median preoptic nucleus), LPO (lateral preoptic area),
1255 MPO (medial preoptic area).

1256 **References**

- 1257 Alexa, A., Rahnenfuhrer, J., 2020. topGO: Enrichment Analysis for Gene Ontology.
- 1258 Anderson, S.A., Eisenstat, D.D., Shi, L., Rubenstein, J.L.R., 1997. Interneuron Migration
1259 from Basal Forebrain to Neocortex: Dependence on Dlx Genes. *Science* 278,
1260 474–476. <https://doi.org/10.1126/science.278.5337.474>
- 1261 Andrews, S., 2010. FastQC: a quality control tool for high throughput sequence data.
- 1262 Angerer, P., Haghverdi, L., Büttner, M., Theis, F.J., Marr, C., Buettner, F., 2016. destiny:
1263 diffusion maps for large-scale single-cell data in R. *Bioinformatics* 32, 1241–
1264 1243. <https://doi.org/10.1093/bioinformatics/btv715>
- 1265 Armoskus, C., Moreira, D., Bollinger, K., Jimenez, O., Taniguchi, S., Tsai, H.-W., 2014.
1266 Identification of sexually dimorphic genes in the neonatal mouse cortex and
1267 hippocampus. *Brain Res.* 1562, 23–38.
1268 <https://doi.org/10.1016/j.brainres.2014.03.017>
- 1269 Asbreuk, C.H.J., van Schaick, H.S.A., Cox, J.J., Kromkamp, M., Smidt, M.P., Burbach,
1270 J.P.H., 2002. The homeobox genes Lhx7 and Gbx1 are expressed in the basal
1271 forebrain cholinergic system. *Neuroscience* 109, 287–298.
- 1272 Batista-Brito, R., Ward, C., Fishell, G., 2020. The generation of cortical interneurons.
1273 *Comprehensive Developmental Neuroscience. Patterning Cell Type Specif. Dev.*
1274 *CNS PNS* 1, 461–480.
- 1275 Beccari, L., Marco-Ferreres, R., Bovolenta, P., 2013. The logic of gene regulatory
1276 networks in early vertebrate forebrain patterning. *Mech. Dev.* 130, 95–111.
1277 <https://doi.org/10.1016/j.mod.2012.10.004>
- 1278 Bedford, L., Walker, R., Kondo, T., van Crüchten, I., King, E.R., Sablitzky, F., 2005. Id4
1279 is required for the correct timing of neural differentiation. *Dev. Biol.* 280, 386–
1280 395. <https://doi.org/10.1016/j.ydbio.2005.02.001>
- 1281 Borello, U., Cobos, I., Long, J.E., Murre, C., Rubenstein, J.L., 2008. FGF15 promotes
1282 neurogenesis and opposes FGF8 function during neocortical development.
1283 *Neural Develop.* 3, 17. <https://doi.org/10.1186/1749-8104-3-17>
- 1284 Breiman, L., 2001. Random Forests. *Mach. Learn.* 45, 5–32.
1285 <https://doi.org/10.1023/A:1010933404324>
- 1286 Butler, A., Hoffman, P., Smibert, P., Papalexi, E., Satija, R., 2018. Integrating single-cell
1287 transcriptomic data across different conditions, technologies, and species. *Nat.*
1288 *Biotechnol.* 36, 411–420. <https://doi.org/10.1038/nbt.4096>

- 1289 Campbell, P., Reep, R.L., Stoll, M.L., Ophir, A.G., Phelps, S.M., 2009. Conservation
1290 and diversity of Foxp2 expression in muroid rodents: Functional implications. *J.*
1291 *Comp. Neurol.* 512, 84–100. <https://doi.org/10.1002/cne.21881>
- 1292 Carlson, M., 2019. *org.Mm.eg.db: Genome wide annotation for Mouse.*
- 1293 Chen, L., Chatterjee, M., Li, J.Y.H., 2010. The mouse homeobox gene Gbx2 is required
1294 for the development of cholinergic interneurons in the striatum. *J. Neurosci. Off.*
1295 *J. Soc. Neurosci.* 30, 14824–14834.
- 1296 Dobin, A., 2013. STAR: ultrafast universal RNA-seq aligner. *Bioinformatics* 29, 15–21.
- 1297 Dunham, I., Kundaje, A., Aldred, S.F., Collins, P.J., Davis, C.A., Doyle, F., Epstein,
1298 C.B., Fritze, S., Harrow, J., Kaul, R., Khatun, J., Lajoie, B.R., Landt, S.G., Lee,
1299 B.-K., Pauli, F., Rosenbloom, K.R., Sabo, P., Safi, A., Sanyal, A., Shores, N.,
1300 Simon, J.M., Song, L., Trinklein, N.D., Altshuler, R.C., Birney, E., Brown, J.B.,
1301 Cheng, C., Djebali, S., Dong, X., Dunham, I., Ernst, J., Furey, T.S., Gerstein, M.,
1302 Giardine, B., Greven, M., Hardison, R.C., Harris, R.S., Herrero, J., Hoffman,
1303 M.M., Iyer, S., Kellis, M., Khatun, J., Kheradpour, P., Kundaje, A., Lassmann, T.,
1304 Li, Q., Lin, X., Marinov, G.K., Merkel, A., Mortazavi, A., Parker, S.C.J., Reddy,
1305 T.E., Rozowsky, J., Schlesinger, F., Thurman, R.E., Wang, J., Ward, L.D.,
1306 Whitfield, T.W., Wilder, S.P., Wu, W., Xi, H.S., Yip, K.Y., Zhuang, J., Bernstein,
1307 B.E., Birney, E., Dunham, I., Green, E.D., Gunter, C., Snyder, M., Pazin, M.J.,
1308 Lowdon, R.F., Dillon, L.A.L., Adams, L.B., Kelly, C.J., Zhang, J., Wexler, J.R.,
1309 Green, E.D., Good, P.J., Feingold, E.A., Bernstein, B.E., Birney, E., Crawford,
1310 G.E., Dekker, J., Elnitski, L., Farnham, P.J., Gerstein, M., Giddings, M.C.,
1311 Gingeras, T.R., Green, E.D., Guigó, R., Hardison, R.C., Hubbard, T.J., Kellis, M.,
1312 Kent, W.J., Lieb, J.D., Margulies, E.H., Myers, R.M., Snyder, M.,
1313 Stamatoyannopoulos, J.A., Tenenbaum, S.A., Weng, Z., White, K.P., Wold, B.,
1314 Khatun, J., Yu, Y., Wrobel, J., Risk, B.A., Gunawardena, H.P., Kuiper, H.C.,
1315 Maier, C.W., Xie, L., Chen, X., Giddings, M.C., Bernstein, B.E., Epstein, C.B.,
1316 Shores, N., Ernst, J., Kheradpour, P., Mikkelsen, T.S., Gillespie, S., Goren, A.,
1317 Ram, O., Zhang, X., Wang, L., Issner, R., Coyne, M.J., Durham, T., Ku, M.,
1318 Truong, T., Ward, L.D., Altshuler, R.C., Eaton, M.L., Kellis, M., Djebali, S., Davis,
1319 C.A., Merkel, A., Dobin, A., Lassmann, T., Mortazavi, A., Tanzer, A., Lagarde, J.,
1320 Lin, W., Schlesinger, F., Xue, C., Marinov, G.K., Khatun, J., Williams, B.A.,
1321 Zaleski, C., Rozowsky, J., Röder, M., Kokocinski, F., Abdelhamid, R.F., Alioto, T.,
1322 Antoshechkin, I., Baer, M.T., Batut, P., Bell, I., Bell, K., Chakraborty, S., Chen,
1323 X., Chrast, J., Curado, J., Derrien, T., Drenkow, J., Dumais, E., Dumais, J.,
1324 Duttagupta, R., Fastuca, M., Fejes-Toth, K., Ferreira, P., Foissac, S., Fullwood,
1325 M.J., Gao, H., Gonzalez, D., Gordon, A., Gunawardena, H.P., Howald, C., Jha,
1326 S., Johnson, R., Kapranov, P., King, B., Kingswood, C., Li, G., Luo, O.J., Park,
1327 E., Preall, J.B., Presaud, K., Ribeca, P., Risk, B.A., Robyr, D., Ruan, X.,
1328 Sammeth, M., Sandhu, K.S., Schaeffer, L., See, L.-H., Shahab, A., Skancke, J.,
1329 Suzuki, A.M., Takahashi, H., Tilgner, H., Trout, D., Walters, N., Wang, H.,
1330 Wrobel, J., Yu, Y., Hayashizaki, Y., Harrow, J., Gerstein, M., Hubbard, T.J.,

- 1331 Reymond, A., Antonarakis, S.E., Hannon, G.J., Giddings, M.C., Ruan, Y., Wold,
1332 B., Carninci, P., Guigó, R., Gingeras, T.R., Rosenbloom, K.R., Sloan, C.A.,
1333 Learned, K., Malladi, V.S., Wong, M.C., Barber, G.P., Cline, M.S., Dreszer, T.R.,
1334 Heitner, S.G., Karolchik, D., Kent, W.J., Kirkup, V.M., Meyer, L.R., Long, J.C.,
1335 Maddren, M., Raney, B.J., Furey, T.S., Song, L., Grassef, L.L., Giresi, P.G.,
1336 Lee, B.-K., Battenhouse, A., Sheffield, N.C., Simon, J.M., Showers, K.A., Safi, A.,
1337 London, D., Bhinge, A.A., Shestak, C., Schaner, M.R., Ki Kim, S., Zhang, Z.Z.,
1338 Mieczkowski, P.A., Mieczkowska, J.O., Liu, Z., McDaniell, R.M., Ni, Y., Rashid,
1339 N.U., Kim, M.J., Adar, S., Zhang, Z., Wang, T., Winter, D., Keefe, D., Birney, E.,
1340 Iyer, V.R., Lieb, J.D., Crawford, G.E., Li, G., Sandhu, K.S., Zheng, M., Wang, P.,
1341 Luo, O.J., Shahab, A., Fullwood, M.J., Ruan, X., Ruan, Y., Myers, R.M., Pauli, F.,
1342 Williams, B.A., Gertz, J., Marinov, G.K., Reddy, T.E., Vielmetter, J., Partridge, E.,
1343 Trout, D., Varley, K.E., Gasper, C., The ENCODE Project Consortium, Overall
1344 coordination (data analysis coordination), Data production leads (data
1345 production), Lead analysts (data analysis), Writing group, NHGRI project
1346 management (scientific management), Principal investigators (steering
1347 committee), Boise State University and University of North Carolina at Chapel Hill
1348 Proteomics groups (data production and analysis), Broad Institute Group (data
1349 production and analysis), Cold Spring Harbor, U. of G., Center for Genomic
1350 Regulation, Barcelona, RIKEN, Sanger Institute, University of Lausanne,
1351 Genome Institute of Singapore group (data production and analysis), Data
1352 coordination center at UC Santa Cruz (production data coordination), Duke
1353 University, E., University of Texas, Austin, University of North Carolina-Chapel
1354 Hill group (data production and analysis), Genome Institute of Singapore group
1355 (data production and analysis), HudsonAlpha Institute, C., UC Irvine, Stanford
1356 group (data production and analysis), 2012. An integrated encyclopedia of DNA
1357 elements in the human genome. *Nature* 489, 57–74.
1358 <https://doi.org/10.1038/nature11247>
- 1359 Eisenstat, D.D., Liu, J.K., Mione, M., Zhong, W., Yu, G., Anderson, S.A., Ghattas, I.,
1360 Puellas, L., Rubenstein, J.L.R., 1999. DLX-1, DLX-2, and DLX-5 expression
1361 define distinct stages of basal forebrain differentiation. *J. Comp. Neurol.* 414,
1362 217–237. [https://doi.org/10.1002/\(SICI\)1096-9861\(19991115\)414:2<217::AID-](https://doi.org/10.1002/(SICI)1096-9861(19991115)414:2<217::AID-CNE6>3.0.CO;2-I)
1363 [CNE6>3.0.CO;2-I](https://doi.org/10.1002/(SICI)1096-9861(19991115)414:2<217::AID-CNE6>3.0.CO;2-I)
- 1364 Elshatory, Y., Gan, L., 2008. The LIM-homeobox gene *Islet-1* is required for the
1365 development of restricted forebrain cholinergic neurons. *J. Neurosci. Off. J. Soc.*
1366 *Neurosci.* 28, 3291–3297.
- 1367 Feng, L., Hatten, M.E., Heintz, N., 1994. Brain lipid-binding protein (BLBP): A novel
1368 signaling system in the developing mammalian CNS. *Neuron* 12, 895–908.
1369 [https://doi.org/10.1016/0896-6273\(94\)90341-7](https://doi.org/10.1016/0896-6273(94)90341-7)
- 1370 Flames, N., Pla, R., Gelman, D.M., Rubenstein, J.L.R., Puellas, L., Marín, O., 2007.
1371 Delineation of multiple subpallial progenitor domains by the combinatorial

- 1372 expression of transcriptional codes. *J. Neurosci. Off. J. Soc. Neurosci.* 27, 9682–
1373 9695.
- 1374 Flandin, P., Kimura, S., Rubenstein, J.L.R., 2010. The progenitor zone of the ventral
1375 medial ganglionic eminence requires Nkx2-1 to generate most of the globus
1376 pallidus but few neocortical interneurons. *J. Neurosci. Off. J. Soc. Neurosci.* 30,
1377 2812–2823.
- 1378 Fragkouli, A., Wijk, N.V. van, Lopes, R., Kessarlis, N., Pachnis, V., 2009. LIM
1379 homeodomain transcription factor-dependent specification of bipotential MGE
1380 progenitors into cholinergic and GABAergic striatal interneurons. *Development*
1381 136, 3841–3851. <https://doi.org/10.1242/dev.038083>
- 1382 Hafemeister, C., Satija, R., 2019. Normalization and variance stabilization of single-cell
1383 RNA-seq data using regularized negative binomial regression. *Genome Biol.* 20,
1384 296. <https://doi.org/10.1186/s13059-019-1874-1>
- 1385 Haubensak, W., Attardo, A., Denk, W., Huttner, W.B., 2004. Neurons arise in the basal
1386 neuroepithelium of the early mammalian telencephalon: A major site of
1387 neurogenesis. *Proc. Natl. Acad. Sci.* 101, 3196–3201.
1388 <https://doi.org/10.1073/pnas.0308600100>
- 1389 Hoch, R.V., Clarke, J.A., Rubenstein, J.L.R., 2015a. Fgf signaling controls the
1390 telencephalic distribution of Fgf-expressing progenitors generated in the rostral
1391 patterning center. *Neural Develop.* 10, 8–15.
- 1392 Hoch, R.V., Lindtner, S., Price, J.D., Rubenstein, J.L.R., 2015b. OTX2 Transcription
1393 Factor Controls Regional Patterning within the Medial Ganglionic Eminence and
1394 Regional Identity of the Septum. *Cell Rep.* 12, 482–494.
- 1395 Hu, J.S., Vogt, D., Lindtner, S., Sandberg, M., Silberberg, S.N., Rubenstein, J.L.R.,
1396 2017. Coup-TF1 and Coup-TF2 control subtype and laminar identity of MGE-
1397 derived neocortical interneurons. *Dev. Camb. Engl.* 144, 2837–2851.
- 1398 Inoue, T., Ota, M., Ogawa, M., Mikoshiba, K., Aruga, J., 2007. Zic1 and Zic3 Regulate
1399 Medial Forebrain Development through Expansion of Neuronal Progenitors. *J.*
1400 *Neurosci.* 27, 5461–5473. <https://doi.org/10.1523/JNEUROSCI.4046-06.2007>
- 1401 J.L.R., R., Campbell, K., 2020. Neurogenesis in the basal ganglia. *Comprehensive*
1402 *Developmental Neuroscience. Patterning Cell Type Specif. Dev. CNS PNS* 1,
1403 399–403.
- 1404 Kageyama, R., Ohtsuka, T., Kobayashi, T., 2008. Roles of Hes genes in neural
1405 development. *Dev. Growth Differ.* 50 Suppl 1, S97-103.

- 1406 Kessaris, N., Magno, L., Rubin, A.N., Oliveira, M.G., 2014. Genetic programs controlling
1407 cortical interneuron fate. *Curr. Opin. Neurobiol.*, SI: Inhibition: Synapses,
1408 *Neurons and Circuits* 26, 79–87. <https://doi.org/10.1016/j.conb.2013.12.012>
- 1409 Kolde, R., 2015. pheatmap: Pretty heatmaps.
- 1410 Kowalczyk, M.S., Tirosh, I., Heckl, D., Rao, T.N., Dixit, A., Haas, B.J., Schneider, R.K.,
1411 Wagers, A.J., Ebert, B.L., Regev, A., 2015. Single-cell RNA-seq reveals changes
1412 in cell cycle and differentiation programs upon aging of hematopoietic stem cells.
1413 *Genome Res.* 25, 1860–1872. <https://doi.org/10.1101/gr.192237.115>
- 1414 Lein, E.S., Hawrylycz, M.J., Ao, N., Ayres, M., Bensinger, A., Bernard, A., Boe, A.F.,
1415 Boguski, M.S., Brockway, K.S., Byrnes, E.J., Chen, Lin, Chen, Li, Chen, T.-M.,
1416 Chi Chin, M., Chong, J., Crook, B.E., Czaplinska, A., Dang, C.N., Datta, S., Dee,
1417 N.R., Desaki, A.L., Desta, T., Diep, E., Dolbeare, T.A., Donelan, M.J., Dong, H.-
1418 W., Dougherty, J.G., Duncan, B.J., Ebbert, A.J., Eichele, G., Estin, L.K., Faber,
1419 C., Facer, B.A., Fields, R., Fischer, S.R., Fliss, T.P., Frensley, C., Gates, S.N.,
1420 Glattfelder, K.J., Halverson, K.R., Hart, M.R., Hohmann, J.G., Howell, M.P.,
1421 Jeung, D.P., Johnson, R.A., Karr, P.T., Kawal, R., Kidney, J.M., Knapik, R.H.,
1422 Kuan, C.L., Lake, J.H., Laramie, A.R., Larsen, K.D., Lau, C., Lemon, T.A., Liang,
1423 A.J., Liu, Y., Luong, L.T., Michaels, J., Morgan, J.J., Morgan, R.J., Mortrud, M.T.,
1424 Mosqueda, N.F., Ng, L.L., Ng, R., Orta, G.J., Overly, C.C., Pak, T.H., Parry, S.E.,
1425 Pathak, S.D., Pearson, O.C., Puchalski, R.B., Riley, Z.L., Rockett, H.R.,
1426 Rowland, S.A., Royall, J.J., Ruiz, M.J., Sarno, N.R., Schaffnit, K., Shapovalova,
1427 N.V., Sivasay, T., Slaughterbeck, C.R., Smith, S.C., Smith, K.A., Smith, B.I., Sodt,
1428 A.J., Stewart, N.N., Stumpf, K.-R., Sunkin, S.M., Sutram, M., Tam, A., Teemer,
1429 C.D., Thaller, C., Thompson, C.L., Varnam, L.R., Visel, A., Whitlock, R.M.,
1430 Wohnoutka, P.E., Wolkey, C.K., Wong, V.Y., Wood, M., Yaylaoglu, M.B., Young,
1431 R.C., Youngstrom, B.L., Feng Yuan, X., Zhang, B., Zwingman, T.A., Jones, A.R.,
1432 2007. Genome-wide atlas of gene expression in the adult mouse brain. *Nature*
1433 445, 168–176. <https://doi.org/10.1038/nature05453>
- 1434 Levine, M., 2008. A systems view of Drosophila segmentation. *Genome Biol.* 9, 207.
1435 <https://doi.org/10.1186/gb-2008-9-2-207>
- 1436 Liao, Y., Smyth, G.K., Shi, W., 2014. featureCounts: an efficient general purpose
1437 program for assigning sequence reads to genomic features. *Bioinformatics* 30,
1438 923–930.
- 1439 Lim, L., Mi, D., Llorca, A., Marín, O., 2018. Development and Functional Diversification
1440 of Cortical Interneurons. *Neuron* 100, 294–313.
1441 <https://doi.org/10.1016/j.neuron.2018.10.009>
- 1442 Lindtner, S., Catta-Preta, R., Tian, H., Su-Feher, L., Price, J.D., Dickel, D.E., Greiner,
1443 V., Silberberg, S.N., McKinsey, G.L., McManus, M.T., Pennacchio, L.A., Visel, A.,
1444 Nord, A.S., Rubenstein, J.L.R., 2019. Genomic Resolution of DLX-Orchestrated

- 1445 Transcriptional Circuits Driving Development of Forebrain GABAergic Neurons.
1446 Cell Rep. 28, 2048-2063.e8. <https://doi.org/10.1016/j.celrep.2019.07.022>
- 1447 Long, J.E., Garel, S., Alvarez-Dolado, M., Yoshikawa, K., Osumi, N., Alvarez-Buylla, A.,
1448 Rubenstein, J.L.R., 2007. Dlx-Dependent and -Independent Regulation of
1449 Olfactory Bulb Interneuron Differentiation. J. Neurosci. 27, 3230–3243.
1450 <https://doi.org/10.1523/JNEUROSCI.5265-06.2007>
- 1451 Long, J.E., Swan, C., Liang, W.S., Cobos, I., Potter, G.B., Rubenstein, J.L.R., 2009.
1452 Dlx1&2 and Mash1 transcription factors control striatal patterning and
1453 differentiation through parallel and overlapping pathways. J. Comp. Neurol. 512,
1454 556–572.
- 1455 Madisen, L., Zwingman, T.A., Sunkin, S.M., Oh, S.W., Zariwala, H.A., Gu, H., Ng, L.L.,
1456 Palmiter, R.D., Hawrylycz, M.J., Jones, A.R., Lein, E.S., Zeng, H., 2010. A robust
1457 and high-throughput Cre reporting and characterization system for the whole
1458 mouse brain. Nat. Neurosci. 13, 133–140.
- 1459 Magno, L., Barry, C., Schmidt-Hieber, C., Theodotou, P., Häusser, M., Kessaris, N.,
1460 2017. NKX2-1 Is Required in the Embryonic Septum for Cholinergic System
1461 Development, Learning, and Memory. Cell Rep. 20, 1572–1584.
- 1462 Marín, O., Anderson, S.A., Rubenstein, J.L.R., 2000. Origin and Molecular Specification
1463 of Striatal Interneurons. J. Neurosci. 20, 6063–6076.
1464 <https://doi.org/10.1523/JNEUROSCI.20-16-06063.2000>
- 1465 Mayer, C., Hafemeister, C., Bandler, R.C., Machold, R., Batista Brito, R., Jaglin, X.,
1466 Allaway, K., Butler, A., Fishell, G., Satija, R., 2018. Developmental diversification
1467 of cortical inhibitory interneurons. Nature 555, 457–462.
1468 <https://doi.org/10.1038/nature25999>
- 1469 McGinnis, C.S., Patterson, D.M., Winkler, J., Conrad, D.N., Hein, M.Y., Srivastava, V.,
1470 Hu, J.L., Murrow, L.M., Weissman, J.S., Werb, Z., Chow, E.D., Gartner, Z.J.,
1471 2019. MULTI-seq: sample multiplexing for single-cell RNA sequencing using
1472 lipid-tagged indices. Nat. Methods 16, 619–626.
- 1473 McGregor, M.M., McKinsey, G.L., Girasole, A.E., Bair-Marshall, C.J., Rubenstein,
1474 J.L.R., Nelson, A.B., 2019. Functionally Distinct Connectivity of Developmentally
1475 Targeted Striosome Neurons. Cell Rep. 29, 1419-1428.e5.
1476 <https://doi.org/10.1016/j.celrep.2019.09.076>
- 1477 McInnes, L., Healy, J., Saul, N., Großberger, L., 2018. UMAP: Uniform Manifold
1478 Approximation and Projection. J. Open Source Softw. 3, 861.
1479 <https://doi.org/10.21105/joss.00861>

- 1480 Mckinsey, G.L., Lindtner, S., Trzcinski, B., Visel, A., Pennacchio, L.A., Huylebroeck, D.,
1481 Higashi, Y., Rubenstein, J.L.R., 2013. Dlx1&2-dependent expression of Zfhx1b
1482 (Sip1, Zeb2) regulates the fate switch between cortical and striatal interneurons.
1483 Neuron 77, 83–98.
- 1484 Mi, D., Li, Z., Lim, L., Li, M., Moissidis, M., Yang, Y., Gao, T., Hu, T.X., Pratt, T., Price,
1485 D.J., Sestan, N., Marín, O., 2018. Early emergence of cortical interneuron
1486 diversity in the mouse embryo. Science 360, 81–85.
1487 <https://doi.org/10.1126/science.aar6821>
- 1488 Nóbrega-Pereira, S., Gelman, D., Bartolini, G., Pla, R., Pierani, A., Marín, O., 2010.
1489 Origin and Molecular Specification of Globus Pallidus Neurons. J. Neurosci. 30,
1490 2824–2834. <https://doi.org/10.1523/JNEUROSCI.4023-09.2010>
- 1491 Nord, A.S., 2015. Learning about mammalian gene regulation from functional enhancer
1492 assays in the mouse. Genomics, Recent advances in functional assays of
1493 transcriptional enhancers 106, 178–184.
1494 <https://doi.org/10.1016/j.ygeno.2015.06.008>
- 1495 Nord, A.S., 2013. Rapid and pervasive changes in genome-wide enhancer usage during
1496 mammalian development. Cell 155, 1521–1531.
- 1497 Pai, E.L.-L., Vogt, D., Clemente-Perez, A., Mckinsey, G.L., Cho, F.S., Hu, J.S., Wimer,
1498 M., Paul, A., Fazel Darbandi, S., Pla, R., Nowakowski, T.J., Goodrich, L.V., Paz,
1499 J.T., Rubenstein, J.L.R., 2019. Mafk and c-Maf Have Prenatal Compensatory
1500 and Postnatal Antagonistic Roles in Cortical Interneuron Fate and Function. Cell
1501 Rep. 26, 1157-1173.e5.
- 1502 Pattabiraman, K., Golonzhka, O., Lindtner, S., Nord, A.S., Taher, L., Hoch, R.,
1503 Silberberg, S.N., Zhang, D., Chen, B., Zeng, H., Pennacchio, L.A., Puelles, L.,
1504 Visel, A., Rubenstein, J.L.R., 2014. Transcriptional Regulation of Enhancers
1505 Active in Protodomains of the Developing Cerebral Cortex. Neuron 82, 989–
1506 1003. <https://doi.org/10.1016/j.neuron.2014.04.014>
- 1507 Petryniak, M.A., Potter, G.B., Rowitch, D.H., Rubenstein, J.L.R., 2007. Dlx1 and Dlx2
1508 control neuronal versus oligodendroglial cell fate acquisition in the developing
1509 forebrain. Neuron 55, 417–433.
- 1510 Picard Toolkit, 2019. . Broad Institute, GitHub Repository.
- 1511 Porteus, M.H., Bulfone, A., Liu, J.K., Puelles, L., Lo, L.C., Rubenstein, J.L., 1994. DLX-
1512 2, MASH-1, and MAP-2 expression and bromodeoxyuridine incorporation define
1513 molecularly distinct cell populations in the embryonic mouse forebrain. J.
1514 Neurosci. 14, 6370–6383. [https://doi.org/10.1523/JNEUROSCI.14-11-](https://doi.org/10.1523/JNEUROSCI.14-11-06370.1994)
1515 06370.1994

- 1516 Preibisch, S., Saalfeld, S., Tomancak, P., 2009. Globally optimal stitching of tiled 3D
1517 microscopic image acquisitions. *Bioinformatics* 25, 1463–1465.
- 1518 Puelles, L., Harrison, M., Paxinos, G., Watson, C., 2013. A developmental ontology for
1519 the mammalian brain based on the prosomeric model. *Trends Neurosci.* 36, 570–
1520 578. <https://doi.org/10.1016/j.tins.2013.06.004>
- 1521 Puelles, L., Morales-Delgado, N., Merchán, P., Castro-Robles, B., Martínez-de-la-Torre,
1522 M., Díaz, C., Ferran, J.L., 2016. Radial and tangential migration of telencephalic
1523 somatostatin neurons originated from the mouse diagonal area. *Brain Struct.*
1524 *Funct.* 221, 3027–3065.
- 1525 Reddington, J.P., Garfield, D.A., Sigalova, O.M., Karabacak Calviello, A., Marco-
1526 Ferreres, R., Girardot, C., Viales, R.R., Degner, J.F., Ohler, U., Furlong, E.E.M.,
1527 2020. Lineage-Resolved Enhancer and Promoter Usage during a Time Course of
1528 Embryogenesis. *Dev. Cell* 55, 648-664.e9.
1529 <https://doi.org/10.1016/j.devcel.2020.10.009>
- 1530 Roychoudhury, K., Salomone, J., Qin, S., Cain, B., Adam, M., Potter, S.S., Nakafuku,
1531 M., Gebelein, B., Campbell, K., 2020. Physical interactions between *Gsx2* and
1532 *Ascl1* balance progenitor expansion versus neurogenesis in the mouse lateral
1533 ganglionic eminence. *Dev. Camb. Engl.* 147, dev185348.
- 1534 Rubin, A.N., Alfonsi, F., Humphreys, M.P., Choi, C.K.P., Rocha, S.F., Kessaris, N.,
1535 2010. The Germinal Zones of the Basal Ganglia But Not the Septum Generate
1536 GABAergic Interneurons for the Cortex. *J. Neurosci.* 30, 12050–12062.
1537 <https://doi.org/10.1523/JNEUROSCI.6178-09.2010>
- 1538 Sanchez-Ortiz, E., Yui, D., Song, D., Li, Y., Rubenstein, J.L., Reichardt, L.F., Parada,
1539 L.F., 2012. *TrkA* Gene Ablation in Basal Forebrain Results in Dysfunction of the
1540 Cholinergic Circuitry. *J. Neurosci.* 32, 4065–4079.
1541 <https://doi.org/10.1523/JNEUROSCI.6314-11.2012>
- 1542 Sandberg, M., Flandin, P., Silberberg, S., Su-Feher, L., Price, J.D., Hu, J.S., Kim, C.,
1543 Visel, A., Nord, A.S., Rubenstein, J.L.R., 2016. Transcriptional Networks
1544 Controlled by *NKX2-1* in the Development of Forebrain GABAergic Neurons.
1545 *Neuron* 91, 1260–1275. <https://doi.org/10.1016/j.neuron.2016.08.020>
- 1546 Silberberg, S.N., Taher, L., Lindtner, S., Sandberg, M., Nord, A.S., Vogt, D., McKinsey,
1547 G.L., Hoch, R., Pattabiraman, K., Zhang, D., Ferran, J.L., Rajkovic, A.,
1548 Golonzhka, O., Kim, C., Zeng, H., Puelles, L., Visel, A., Rubenstein, J.L.R., 2016.
1549 Subpallial Enhancer Transgenic Lines: a Data and Tool Resource to Study
1550 Transcriptional Regulation of GABAergic Cell Fate. *Neuron* 92, 59–74.
1551 <https://doi.org/10.1016/j.neuron.2016.09.027>

- 1552 Stuart, T., Butler, A., Hoffman, P., Hafemeister, C., Papalexi, E., Mauck, W.M., Hao, Y.,
1553 Stoeckius, M., Smibert, P., Satija, R., 2019. Comprehensive Integration of Single-
1554 Cell Data. *Cell* 177, 1888-1902.e21. <https://doi.org/10.1016/j.cell.2019.05.031>
- 1555 Visel, A., Taher, L., Girgis, H., May, D., Golonzhka, O., Hoch, R.V., McKinsey, G.L.,
1556 Pattabiraman, K., Silberberg, S.N., Blow, M.J., Hansen, D.V., Nord, A.S.,
1557 Akiyama, J.A., Holt, A., Hosseini, R., Phouanavong, S., Plajzer-Frick, I.,
1558 Shoukry, M., Afzal, V., Kaplan, T., Kriegstein, A.R., Rubin, E.M., Ovcharenko, I.,
1559 Pennacchio, L.A., Rubenstein, J.L.R., 2013. A High-Resolution Enhancer Atlas of
1560 the Developing Telencephalon. *Cell* 152, 895–908.
1561 <https://doi.org/10.1016/j.cell.2012.12.041>
- 1562 Wang, L., Wang, S., Li, W., 2012. RSeQC: quality control of RNA-seq experiments.
1563 *Bioinformatics* 28, 2184–2185.
- 1564 Yun, K., Mantani, A., Garel, S., Rubenstein, J., Israel, M.A., 2004. Id4 regulates neural
1565 progenitor proliferation and differentiation in vivo. *Development* 131, 5441–5448.
1566 <https://doi.org/10.1242/dev.01430>
- 1567 Yuzwa, S.A., Borrett, M.J., Innes, B.T., Voronova, A., Ketela, T., Kaplan, D.R., Bader,
1568 G.D., Miller, F.D., 2017. Developmental Emergence of Adult Neural Stem Cells
1569 as Revealed by Single-Cell Transcriptional Profiling. *Cell Rep.* 21, 3970–3986.
- 1570 Zeisel, A., Hochgerner, H., Lönnerberg, P., Johnsson, A., Memic, F., van der Zwan, J.,
1571 Häring, M., Braun, E., Borm, L.E., La Manno, G., Codeluppi, S., Furlan, A., Lee,
1572 K., Skene, N., Harris, K.D., Hjerling-Leffler, J., Arenas, E., Ernfors, P., Marklund,
1573 U., Linnarsson, S., 2018. Molecular Architecture of the Mouse Nervous System.
1574 *Cell* 174, 999-1014.e22. <https://doi.org/10.1016/j.cell.2018.06.021>
- 1575 Zheng, G.X.Y., Terry, J.M., Belgrader, P., Ryvkin, P., Bent, Z.W., Wilson, R., Ziraldo,
1576 S.B., Wheeler, T.D., McDermott, G.P., Zhu, J., Gregory, M.T., Shuga, J.,
1577 Montesclaros, L., Underwood, J.G., Masquelier, D.A., Nishimura, S.Y., Schnall-
1578 Levin, M., Wyatt, P.W., Hindson, C.M., Bharadwaj, R., Wong, A., Ness, K.D.,
1579 Beppu, L.W., Deeg, H.J., McFarland, C., Loeb, K.R., Valente, W.J., Ericson,
1580 N.G., Stevens, E.A., Radich, J.P., Mikkelsen, T.S., Hindson, B.J., Bielas, J.H.,
1581 2017. Massively parallel digital transcriptional profiling of single cells. *Nat.*
1582 *Commun.* 8, 14049. <https://doi.org/10.1038/ncomms14049>
- 1583